NATIONAL AERONAUTICS AND SPACE ADMINISTRATION

Technical Report 32-1578

Results of Solar Electric Thrust Vector Control System Design, Development, and Tests

G. E. Fleischer

JET PROPULSION LABORATORY
CALIFORNIA INSTITUTE OF TECHNOLOGY
PASADENA, CALIFORNIA

February 15, 1973

NATIONAL AERONAUTICS AND SPACE ADMINISTRATION

Technical Report 32-1578

Results of Solar Electric Thrust Vector Control System Design, Development, and Tests

G. E. Fleischer

JET PROPULSION LABORATORY
CALIFORNIA INSTITUTE OF TECHNOLOGY
PASADENA, CALIFORNIA

February 15, 1973

Prepared Under Contract No. NAS 7-100
National Aeronautics and Space Administration

Preface

The work described in this report was performed by the Guidance and Control Division of the Jet Propulsion Laboratory.

Acknowledgment

The technical support and contributions of JPL personnel which made this report possible are gratefully acknowledged. William Crawford, in particular, provided valuable aid with the TVCS electronics, the design and development of which he directed most successfully. Gerald Perkins, John Ferrera, and Lee Brimmer of the Spacecraft Control Section were also helpful during the testing periods.

Thanks must also go to Tom Masek, Tad Macie, and Daniel Kerrisk of the Propulsion Division (Research and Advanced Concepts Section), Henry Doupé, Carl Love, and Robert Soden of the Data Systems Division, and James Bryant and Ronald Ross of the Engineering Mechanics Division for their valuable help and advice.

Contents

Tables

Figures

Contents (contd)

Figures (contd)

Contents (contd)

Figures (contd)

Contents (contd)

Figures (contd)

"Page missing from available version"

PAGES 1 — 6
MISSING !

Since $\sigma_2 = \sigma_3$ (and assuming $\xi_2 = \xi_3$),

$$\frac{\theta_{fy}(S)}{T_y(S)} = \frac{S^2 + 2\xi_2\sigma_2 S + \sigma_2^2}{I_{yy}^* S^2\left[\left(1 - \frac{96.64}{I_{yy}^*}\right)S^2 + 2\xi_2\sigma_2 S + \sigma_2^2\right]}$$

$$\frac{\theta_{fz}(S)}{T_z(S)} = \frac{S^2 + 2\xi_1\sigma_1 S + \sigma_1^2}{I_{zz}^* S^2\left[\left(1 - \frac{150.33^2}{I_{zz}^*}\right)S^2 + 2\xi_1\sigma_1 S + \sigma_1^2\right]}$$

These transfer functions then represent the effects of the fundamental solar array bending modes on the rotational response of the rigid bus. One additional simplification was made before incorporating these models into the analog computer simulation of vehicle dynamics. Since the quantity $(1 - 96.64/I_{yy}^*)$ is very nearly 1, meaning that the structural pole and zero contributed by the solar array to the y-axis loop are very nearly coincident, virtually no structural effects on control response should be expected from this mode. It was therefore eliminated.

The complete analog computer simulation program for the attitude dynamics (including scaling) is shown in Fig. 13. The simulation required the use of five electronic (diode "quarter-square") multipliers, 13 integrators, 36 summing or inverting amplifiers, approximately 35 potentiometers, and a Brush Instruments strip-chart recorder.

F. Some Closed-Loop TVCS Test Responses

Figures 14 and 15 show the recorded responses of several variables within the TVCS (modified as discussed in Sections IC and ID) for a test run with initial translator and gimbal position offsets. In the case of the translator, the position offsets are analogous to and indistinguishable from center-of-mass misalignments in the x- and y-direction. Initial values were $y_T = 0.0213$ m (0.07 ft), $x_T = -0.0244$ m (-0.08 ft), and $\alpha = 0.095$ rad.

The transient responses of the x- and y-axes, as controlled by the y-translator and x-translator, respectively, were nicely damped and therefore quite satisfactory. The "glitch" in $y_T(t)$ at about 310 s is as yet unexplained, although there is some suspicion that it was the result of a power switching transient to the ion engine bank operating in the vacuum chamber. (Such power transients had been observed once or twice earlier to couple enough energy to some TVCS cables to momentarily send a short burst of pulses to one or another TVC actuator.) Note also the roughly 10 times greater y-axis response magnitudes than in the x-axis, a consequence, as mentioned earlier, of dropping the y-axis sensor gain by a factor of 10 to compensate for about 10 times less inertia. VCO and compensation loop parameters were the same for both translator loops.

The gimbaled z-axis response obviously was not well damped and therefore somewhat less than satisfactory in performance. A look at the linearized z-axis loop root loci in Fig. 16 shows the actual operating point for the test run results of Figs. 14 and 15. With either one or both outer gimbaled engines operating, the damping factor on the main locus is a rather poor 0.24. The root loci shown correspond to the gimbal loop control parameters used in the test simulation, which are:

$\tau_1 = 500$ s	$K_2 = 3.65$
$\tau_2 = 440$ s	$K_P = 0.50$
$\tau_S = 0.1$ s	$K_{VCO} = 50$ step/s/V
$K_1 = 1.0$ V/step/s	$K_S = 295$ V/rad

(The translator loop root loci are as shown in Fig. 4.) It is obvious that the value of K_2 in particular was poorly chosen for the gimbal loop, and K_P could also be modified somewhat to good effect. In fact, by using $K_2 = 7.0$, $K_P = 0.35$, and all other parameters unchanged, a much improved operating point in the S-plane is produced, as shown in Fig. 17. [For the gimbal loop, $F = 0.057$ N-m/rad (0.0424 ft lb/rad) and $K_M = 0.97\ (10^{-4})$ rad/step.] The transient response for such a modification will be shown in the Section IH digital computer simulations. However, no adjustments of that kind were made in the TVCS gimbal loop electronic hardware, and the remaining test run results reflect the poorly damped gimbal responses.

Figure 18 is another recording of the TVCS response to initial translator and gimbal displacements, showing the pitch phase-plane transient. Of particular interest in this x–y plot is the very evident effect of analog computer integrator drift during the test. When the phase-plane trajectory (which starts at $\dot{\theta}_x = 0$, $\theta_{fx} = 0$) first crosses the $\dot{\theta}_x = 0$ line at about $t = 470$ s, the requirement that the slope of the curve be infinite is very nearly met, although there is a slight positive bias (drift) in the rate. However, at the next apparent crossing ($t \cong 1500$ s), the proper rate/position relationships are obviously not present, an indication of significant levels of drift in both the rate and position integrators.

One further clarification of the results shown in Figs. 14, 15, and 18 is required. Vehicle bus rotations about the x- and z-axes are labeled θ_{fx} and θ_{fz}, respectively (see Fig. 13) and *do* include the effect of solar array vibrations, although no effects are visible. However, because of the manner in which the solar array transfer functions happened to be programmed (see Fig. 13), i.e., inserted between position variables θ_x and θ_{fx} (or θ_z and θ_{fz}), the true bus angular rates $\dot{\theta}_{fx}$ and $\dot{\theta}_{fz}$ were not available. As a result, $\dot{\theta}_x$ and $\dot{\theta}_z$ were recorded instead, actually representing the bus' rotational rates *minus* the perturbing vibrations of the array appendages. These perturbations in rate, though, were quite small and will be shown in the digital computer simulations of Section IH. The variables $\dot{\theta}_y$ and θ_y are strictly rigid-body responses, since appendage modes of vibration were not included in this axis.

At the conclusion of the TVCS transient test response to initial engine displacements ($t \cong 2500$ s), an engine-out condition was simulated by instantaneously setting $f_2 = 0$. The TVCS response to that action was recorded, and the actual strip charts are shown in Figs. 19 and 20.

Engine gimbal angle and roll angular position remained reasonably quiescent during the engine-out transient, as they should, in spite of the 50% reduction in effective roll control torque. Translator displacements [each is required to move 0.114 m (0.375 ft) to put the resultant thrust vector through the vehicle c.m.] were well damped, as predicted by the linear analysis (Fig. 3). And response time of the translator loops was predictably slowed as a result of the smaller control forces and the accompanying lower loop gains. Total translator excursions during the transient were less than 0.183 m (0.6 ft) out of a total available travel of 0.67 m (2.2 ft). The peak pitch angle excursion of the vehicle during the transient was 2.3 deg.

G. Test Problems

Because of the likelihood of continued TVCS hardware tests occurring in the immediate future, it may prove valuable to recount some of the operational difficulties experienced thus far in the hope that at least some of these may be overcome.

Insofar as the TVCS portions of the SEPST III tests are concerned, the simulations were strictly a one-man, part-time (approximately half-time) operation spread over roughly a 4-month period. At the same time, a great deal of effort in terms of man-hours was understandably devoted to ion engine vacuum chamber tests with relatively frequent test shutdowns and system modifications. As a consequence, TVCS closed-loop simulations were, at times, precluded because engine mechanisms could not be moved while the modifications were being effected. While these types of conflicts are inevitable, they do significantly reduce the amount of useful test time and should be planned for.

Without a doubt the most frustrating part of the TVCS tests was simply a consequence of the system's own characteristics. This was the extremely long period of time (usually at least 40 min) necessary to generate just a single transient response from the system. Of course, hand in hand with the slow, real-time TVCS response came the problem of analog integrator drift, which, after 10–15 min of computation time, began to destroy any accurate position–rate relationship in the vehicle dynamics model. The drift degradation of the simulations made them useless for predicting steady-state angular rates or positions of the vehicle. It also goes without saying that the bandwidth of this real-time model made any attempts to use it repetitively as an analytical tool impossible.

The time factor difficulties mentioned above were magnified by a variety of other problems, some of which were probably to be expected. One of these was related primarily to the age of the EAI 231-R analog computer. Now 12 years old, the computer exhibits a number of ills, not the least of which are intermittent patch-board connections. Oxidized, dirty, and sometimes bent contacts and patch-cord pins are the culprits, and it requires some patient searching and experimentation to find the trouble and achieve a reliable patch-board setup.

A faulty electrical connection at the signal patch-board was also the source of lost test time. Several test runs were interrupted by either intermittent or total dropout of the *x*-translator output signal to the analog computer. Although at first the location of the break was unknown, it was ultimately traced to a bad solder connection behind the board. Because of its location, however, the connection was not repairable during the active SEPST III engine test period, and it was necessary to live with the problem for TVCS testing.

Since the simulation control and data recording were done at a site remote from the location of the TVCS hardware, particularly the electronics panel, it was extremely inconvenient and time-consuming to travel back and forth to accomplish such simple tasks as turning the control electronics on and off, resetting or disabling the feedback compensation circuits, or initializing the positions of translator or gimbal mechanisms. It would be quite valuable in future testing to have some capability for remote and automatic control of the system's configuration and initial state.

In general, efficient future testing, at least from the TVCS standpoint, would appear to require better coordination of diverse and often conflicting test objectives and a greatly enhanced capability for automatically controlling the test equipment configuration and operation.

H. Digital Computer Simulations of the Solar Electric TVCS

As a check on the SEPST III TVCS test results, particularly those shown in Figs. 14, 15, 18, 19, and 20, the system equations were programmed for digital computer solution using Continuous System Simulation Language (CSSL III) on the Univac 1108. The vehicle dynamic characteristics were programmed exactly as they were for the analog computer and as they have been described in Sections IA–IE. Control parameter values were, for the most part, taken at their nominal values (e.g., actuator gear ratios, sensor gains) except for a few compensation loop parameter changes of the order of 5% that were made to better reproduce actual test responses.

The digital simulation included only one significant nonlinearity (except for limits on translator/gimbal excursions–limits that were never reached) not shown in the typical control loop block diagram of Fig. 1. This involved a somewhat more accurate simulation of the actual circuit implementation of the time constant τ_1 and associated gain.

The circuit of interest is shown in Fig. 12d, where τ_1 is mechanized using the 100-μf capacitor at the input of operational amplifier *A*. At very low pulse rates (low duty cycle), the impedance of the circuit from the capacitor back through the transistor switch is primarily that of a turned-off switch, or, in other words, infinite. Therefore, the effective time constant is that of the 5-MΩ input resistor and 100-μf capacitor, or 500 s (a number which is used for τ_1 in all the root locus calculations shown in this report). At the other extreme, at the highest pulse rates of the VCO (100% duty cycle), the impedance is that of a turned-on switch in series with 5 MΩ, so that $\tau_1 = 250$ s. (Of course, placing the capacitor in the feedback of amplifier *A* would have prevented these complications, but the problem was not recognized until tests were completed.) Thus, strictly speaking, τ_1 is a function of VCO pulse rate (although $\tau_1 = 500$ s is a good approximation) and so is the dc gain through amplifier *A*. Figure 21 shows the actual functional dependence in the desired transfer function equivalent assuming 25-V pulses, 0.20 s wide, at the transistor switch output. A straight-line approximation to the function shown in Fig. 21, very accurate over the pulse frequency range 0–10 pulses/s, was included in the digital simulation.

Figures 22–32 show the results of a digital simulation of the TVCS test run for the initial engine offsets described in Section IF and in Figs. 14, 15, and 18. Translator and gimbal control loop parameters are those given previously and are consistent with the root loci in Figs. 3 and 16. A program listing for the digital simulation is given in Fig. 33. All transient peaks and their times of occurrence agree quite well with the TVCS test recordings. However, one noticeable difference occurs in the rate of angular position ($\theta_{fx}, \theta_y, \theta_{fz}$) error reduction over the 40+ min simulation period. The analog computer solutions (Figs. 14 and 15) show a much slower reduction, which, as indicated before, is very probably due in large part to the cumulative effect of drift in both the rate and position integrators. There may also be some nonlinear effects occurring in the near-steady-state, limit-cycle-type operation of the control loops, particularly in the VCO (such as bias voltages at the input) feedback compensation loop, and actuators which have not been modeled in enough detail. Remember that the digital program used does not actually deal with discrete pulses but idealizes all system variables as smooth, continuous functions. While the former level of detail could be added, the digital simulation would run at least 10 times more slowly (and 10 times more costly) as a result of its efforts to correctly integrate the effects of thousands of narrow VCO pulses and stepper motor steps.

Notice also the plot of $\dot{\theta}_{fx}(t)$ in Fig. 23 as compared to $\dot{\theta}_x$ in Fig. 22. Except for some very small solar array vibration during the first 4 min, the responses are identical. The plot of $\dot{\theta}_{fz}$ (Fig. 29) shows no noticeable vibration at all.

In Section IF, it was mentioned that a substantial improvement in gimbal loop response could be made by using the values $K_2 = 7.0$ and $K_F = 0.35$. Figures 34–36, results of a digital simulation, demonstrate the improvement over the *z*-axis responses of Figs. 15 and 29–31. Translator loop transient responses were unchanged, since the control axes are effectively independent. Note, however, that the response curve for $\dot{\theta}_{fz}$ now shows some perceptible solar array vibration.

A digital computer simulation was also performed for the "engine-out" TVCS test described in Section IF (see Figs. 19 and 20). Plots of the computer results are given in Figs. 37–45. This simulation is actually a *continuation* of the TVCS response to initial translator and gimbal displacements with f_2 set equal to zero at $t = 2450$ s, just as was done in the actual SEPST III test run. Again, a comparison of the digital computer solutions to the actual test run recordings of Figs. 19 and 20 will show very good agreement throughout the transient period.

I. A Digital Controller and Vehicle Dynamics Simulator for SEPST Testing

Throughout the SEPST III tests, a PDP-11 digital computer was used as a test controller (see Refs. 9 and 10), performing such functions as turning engine power-conditioning equipment on and off, monitoring engine thrust performance, engine failure detection, adjusting thrust levels in relation to pre-stored "flight plans," and simulating various ground commands. Virtually no control was exercised, however, over the functioning of the TVCS electronics, actuators, or analog computer simulation of vehicle dynamics. But the PDP-11 does appear to have the computational capability not only to interact with the TVCS electronics (i.e., for gain switching or monitoring purposes) but actually to *replace* the electronics and perform the thrust vector control function itself.

Space has already been provided in the PDP-11's 8K memory for a prototype subprogram which has been written to perform the per-axis control function shown in Fig. 46. Just like the present TVCS electronics, the computer will receive a simulated celestial sensor error voltage and will derive a sequence of actuator drive pulses as a function of both the sensor error and a feedback compensation signal.

The computer will be capable of updating the pulse output to the actuator drivers every 20 ms. A very simple integration algorithm may be used (such as Euler's Method shown in Fig. 46), since the iteration rate will be extremely fast compared to system time constants.

A basic algorithm for duplicating the TVCS electronics analog functions on a digital computer is shown in Fig. 47. Initial attempts at performing the control function with the PDP-11 will be limited to those functions shown in Fig. 46, first for a single axis and then, hopefully, for all three axes. However, if these tests prove successful and computer storage space permits, the PDP-11's task will be enlarged to include the simulation of vehicle rigid-body dynamics as well (two additional integrations per control axis), including the detailed engine thrust-torque equations.

If the computer is able to handle these functions, a number of current testing problems would be effectively solved. Certainly the problem of analog integrator drift during the long TVCS test runs would be alleviated. Absolute control could easily be maintained over almost all initial conditions of the system variables, and even the initial translator and gimbal positions could be set by computer command rather simply. Complete flexibility with respect to system parameters would be provided; changes would be made by a simple typewriter entry. Even the control law(s) would be changed relatively quickly with only a software modification. Further, the concept of an *on-board* programmable processor for use as a spacecraft attitude controller has already received much support, particularly for extended-life missions (e.g., to the outer planets). One design, the Hybrid Programmable Attitude Control Electronics (HYPACE), is already in the developmental testing stage (Ref. 9) and could be used, among other things, to try out promising solar electric thrust vector control law software with real actuators.

II. A Solar Electric TVCS Using Rate Estimation

A. Linearized System Model

The utility of a state estimation circuit, derived by Kopf (Ref. 12) specifically for the task of estimating the angular rotation rate of a space vehicle, was investigated as it might apply to the same basic solar electric thrust vector control problem discussed in Section I. The estimator, receiving celestial sensor measurements of the space vehicle's angular position, both filters the sensor signal and derives an estimate of vehicle angular rate.

A transfer function block diagram of the proposed single-axis translator (or gimbal) control loop, with estimator, is shown in Fig. 48. Critical parameters associated with the estimator are the filter "time constant" B and the rate-to-position gain K_R. To the extent that the estimator represents a model of the vehicle rigid-body dynamics with corrective feedback through the gains $1/B$ and $1/2B^2$, one has the option of improving the estimation accuracy by introducing a measure of the known applied control torques on the vehicle T_c, divided by the proper inertia constant. However, in the analyses and simulations that follow, this option is foregone as an unnecessary complication. If one sums the rate and position estimates into a single output, the estimator's transfer function has the following form:

$$\frac{V_0(S)}{V_S(S)} = \frac{S^2(2B^2 + BK_R) + S(K_R + 3B) + 1}{(BS + 1)(2B^2S^2 + 2BS + 1)}$$

Factoring the numerator polynomial, the roots are

$$S_1 = -\frac{K_R + 2B}{2B^2 + BK_R}, \qquad S_2 = -\frac{1}{2B + K_R}$$

Assuming that $K_R >> B$, then

$$S_1 \cong -\frac{1}{B}, \qquad S_2 \cong -\frac{1}{K_R}$$

and

$$\frac{V_0(S)}{V_S(S)} \cong \frac{(K_R S + 1)}{2B^2S^2 + 2BS + 1}$$

If the *actual* sensor position signal, rather than the position estimate, is summed with the rate estimate, the transfer function becomes

$$\frac{V_0(S)}{V_S(S)} = \frac{2B^2S^2 + S(K_R + 2B) + 1}{2B^2S^2 + 2BS + 1}$$

If $K_R >> B$, the numerator roots are given approximately by

$$S_1 \cong -\frac{1}{K_R}, \qquad S_2 \cong -\frac{K_R}{2B^2}$$

and

$$\frac{V_0(S)}{V_S(S)} \cong \frac{(K_R S + 1)\left(\frac{2B^2}{K_R} S + 1\right)}{2B^2S^2 + 2BS + 1}$$

In this application, the *filtered* position signal $\hat{V}_S$ will be used to aid in minimizing any potential noise problems at the VCO input. The linearized single-axis open-loop transfer function for the controller with rate estimator (Fig. 48) becomes

$$\frac{T_c(S)}{T(S)} = \frac{FK_M K_S K_{VCO}(\tau_1 S + 1)(K_R S + 1)(S^2 + 2\xi\omega S + \omega^2)}{IS^3(\tau_s S + 1)(\tau_1 S + K_F K_{VCO} + 1)(2B^2S^2 + 2BS + 1)(RS^2 + 2\xi\omega S + \omega^2)}$$

The closed-loop root loci for the single-axis controller shown in Fig. 48 were calculated for a number of parameter variations, and a sample of the results is given in Fig. 49. The parameters used to calculate the loci in Fig. 49 were as follows:

$$B = 1$$

$$K_R = 200 \text{ s}$$

$$K_{VCO} = 50 \text{ pulses/s/V}$$

$$K_F = 0.20$$

$$\tau_1 = 200 \text{ s}$$

$$K_S = 295 \text{ V/rad}$$

$$K_M = 0.64 \times 10^{-4} \text{ m/step } (0.00021 \text{ ft/step})$$

$$F = 0.089\text{–}0.267 \text{ N } (0.02\text{–}0.06 \text{ lb})$$

$$I = 20{,}337 \text{ kg-m}^2 \ (15{,}000 \text{ slug-ft}^2)$$

The celestial sensor time constant was ignored, as were the poles and zeros contributed by the fundamental solar array vibration mode. Good damping is obtained over the entire range of engine thrusts, which was not the case when the controller described in Section I was used. Transient response of the loop, using the translator parameters listed above, to a 0.061-m (0.2-ft) vehicle c.m. offset is shown in Figs. 50–52. The speed of response with the estimator is at least twice that shown in the responses, say in Figs. 23–25, which are for the present controller with less than half the disturbance. Also, the peak angular position transient with the estimator is 1.35 mrad for a 0.061-m (0.2-ft) c.m. offset. With the present controller and a 0.0213-m (0.07-ft) offset, θ error peaks at over 7 mrad.

B. Three-Axis System Simulations

In order to get a more direct comparison between the rate estimating controller and the present scheme, the digital simulation of the complete three-axis system with solar array vibration, used in Section IH, was employed. VCO gain in all three axes was identical at K_{VCO} = 50 pulses/s/V, as was the estimator parameter, $B = 1$. However, the control parameters K_R, τ_1, and K_F were tailored to provide good (although not really optimal) responses in each control axis. The values used are given in Table 3.

Table 3. Rate estimator control parameters for three-axis SEMMS vehicle simulation

Parameter	x-axis	y-axis	z-axis
K_R, s	200	100	250
τ_1, s	200	100	250
K_F, V/pulse/s	0.20	0.30	0.175
K_S, V/rad	250	250	295

Figures 53–61 show system responses to the identical initial conditions present in the SEPST III test and corresponding digital simulation, i.e., initial translator and gimbal position offsets. Comparisons of x- and z-axis responses in particular show the simulated rate estimator loops to be well damped and substantially faster than the present control hardware. In fact, the widened bandwidth in the estimator loop is especially evident in the x-axis response, where solar array perturbations seem to be in somewhat more evidence than before. The gimbal loop (z-axis) response has been drastically improved over that given in Section I as a result of the estimator and proper control parameter choices. Notice also that the low-inertia, yaw axis control loop has had its control parameters (K_R, τ_1, K_F) adjusted to provide good response without lowering the celestial sensor gain K_S, as was done in Section I.

To complete the comparisons, the rate-estimating TVCS was also simulated for the same engine-out condition described in Section I. The resulting transient responses are given in Figs. 62–70. In pitch and yaw (x and y), the translator-controlled axes, recovery from the single-engine shut-down ($f_2 = 0$) is fast and nicely damped. The gimbal axis transient is not nearly as well damped but extremely small in magnitude. (The rate-estimating TVCS simulation program is listed in Fig. 71.)

In summary, the rate-estimating solar electric TVCS certainly promises a vastly improved control capability over the present approach. A control bandwidth improvement by a factor of 2–3 does not seem unreasonable, and yet this still does not threaten to result in any significant solar array interaction problems, much less any serious destabilizing effects.

C. Future Work

The immediate future will see efforts to bench-test a single-axis version of the rate-estimator control loop using real actuators and simulated rigid-vehicle attitude dynamics. It will be necessary to demonstrate that rate-to-position gains on the order of 200–250 s are practical to achieve with conventional circuitry so that these gains, in combination with an estimator time constant of about 1.0 s, do not present noise problems or excessive actuator limit-cycle stepping rates. It does appear, however, that the value of B could be increased substantially if necessary to obtain greater filtering action without significantly altering the system transient response.

In addition, an attempt will be made to program an estimator-TVCS loop on the PDP-11 computer to see if an analog circuit implementation can be dispensed with entirely, along the same lines and for the same reasons discussed in Section I.

References

1. *1975 Jupiter Flyby Mission Using a Solar Electric Propulsion Spacecraft*, Report No. ASD-760-18, Jet Propulsion Laboratory, Pasadena, Calif., March 1968 (JPL internal document).
2. Fleischer, G. E., *Solar Electric Spacecraft Attitude Control System Mechanization*, JPL Eng. Memo. 344-251, March 10, 1970 (JPL internal document).
3. *Solar Electric Multi-Mission Spacecraft (SEMMS) Phase A Final Report (Spacecraft Subsystem Analyses)*, Report No. 617-4, Jet Propulsion Laboratory, Pasadena, Calif., March 3, 1972 (JPL internal document).
4. Crawford, W. E., *A Stepper Motor Drive Electronics for the Solar Electric Thrust Vector Control Subsystem*, JPL Eng. Memo. 344-293, Dec. 2, 1970 (JPL internal document).

References (contd)

5. Crawford, W. E., *Undisturbed Limit Cycle Behavior of the Solar Electric Thrust Vector Control System*, JPL Eng. Memo. 344-287, Oct. 13, 1970 (JPL internal document).

6. Crawford, W. E., March, E. L., Ferrera, J. D., et al., *Solar Electric Propulsion System Integration Technology*, JPL Report 701-173, Vols. 2 and 3 (to be published) (JPL internal document).

7. Marsh, E. L., *Attitude Control–Solar Array Interaction Trade-off Study*, JPL Eng. Memo. 344-381, Aug. 11, 1972 (JPL internal document).

8. Likins, P. W., *Dynamics and Control of Flexible Space Vehicles*, Technical Report 32-1329 (Rev. 1), Jet Propulsion Laboratory, Pasadena, Calif., Jan. 15, 1970.

9. Macie, T. W. and Doupe, H. M., "Automatic Control of an Electric Thrust Subsystem," paper (72-506) presented at AIAA 9th Electric Propulsion Conference, Bethesda, Md., Apr. 17–19, 1972.

10. Doupe, H. M., and Macie, T. W., "Master Controller for an Electric Thrust Subsystem," paper presented at the Fall Symposium of Digital Computer Users' Society, San Francisco, Calif., Nov. 1971.

11. Kopf, E. H., *Hypace Processing Unit—Reference Manual*, JPL Eng. Memo. 344-369, Feb. 2, 1972 (JPL internal document).

12. Kopf, E. H., "A New Approach to Derived Rate," JPL Eng. Memo. 344-317, Feb. 4, 1971 (JPL internal document).

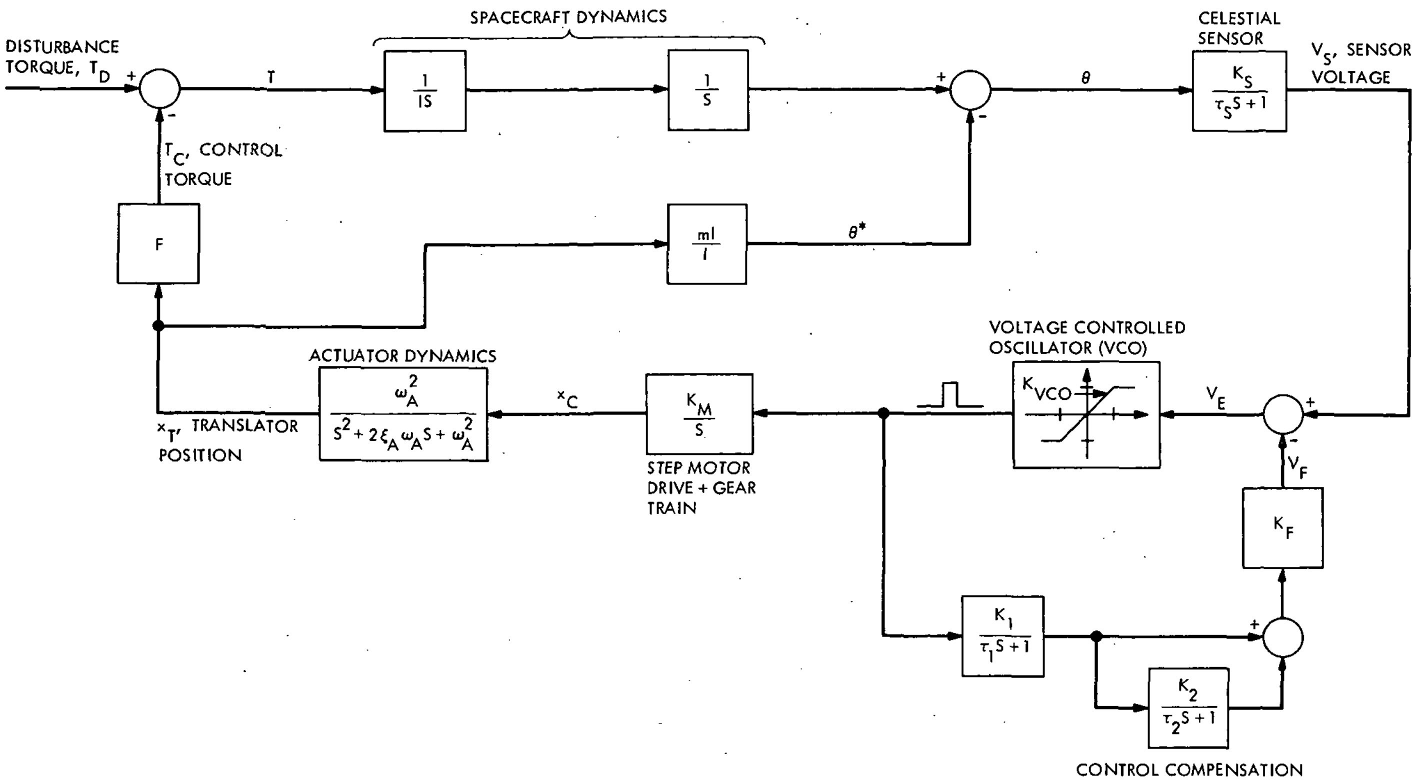

Fig. 1. Single-axis TVCS transfer function block diagram

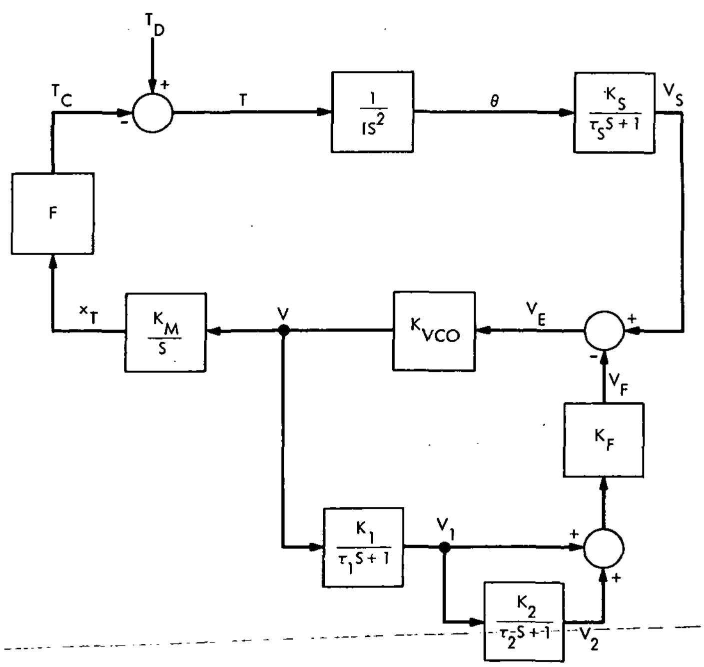

Fig. 2. Simplified TVCS single-axis block diagram

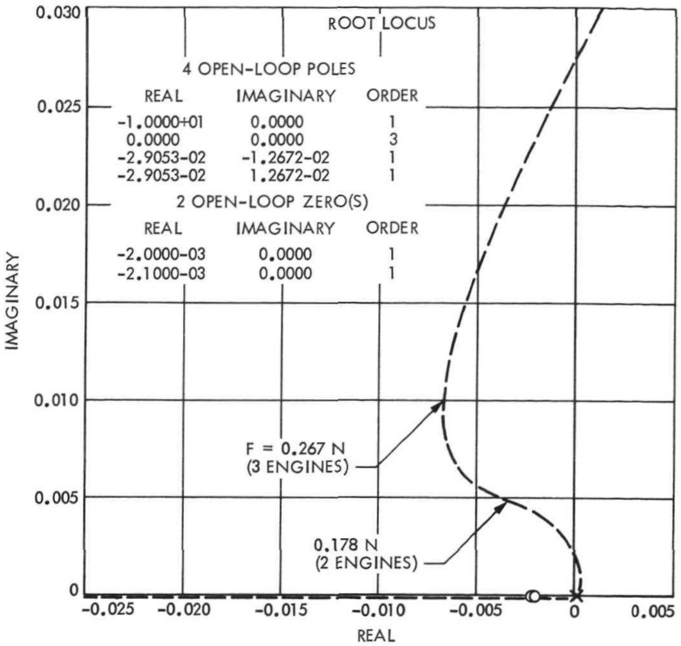

Fig. 3. Closed-loop root loci for the single-axis TVCS (rigid vehicle)

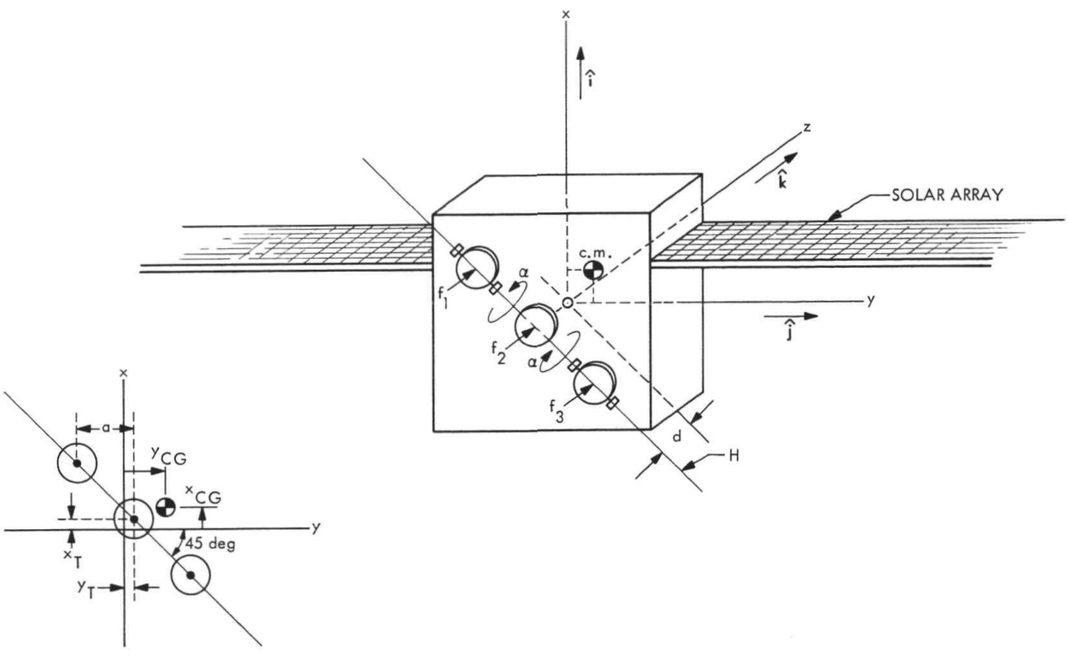

Fig. 4. SEMMS vehicle three-engine configuration

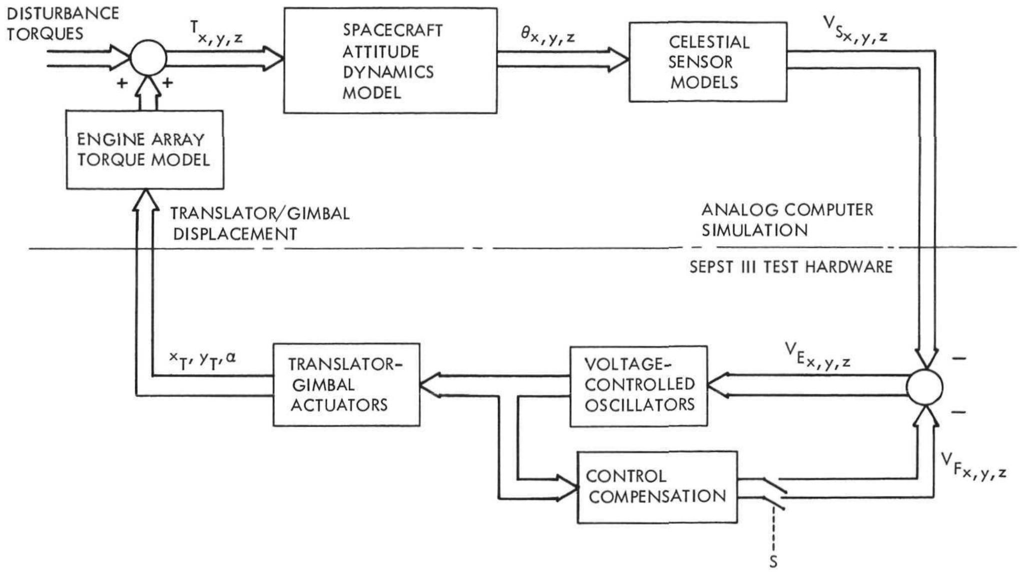

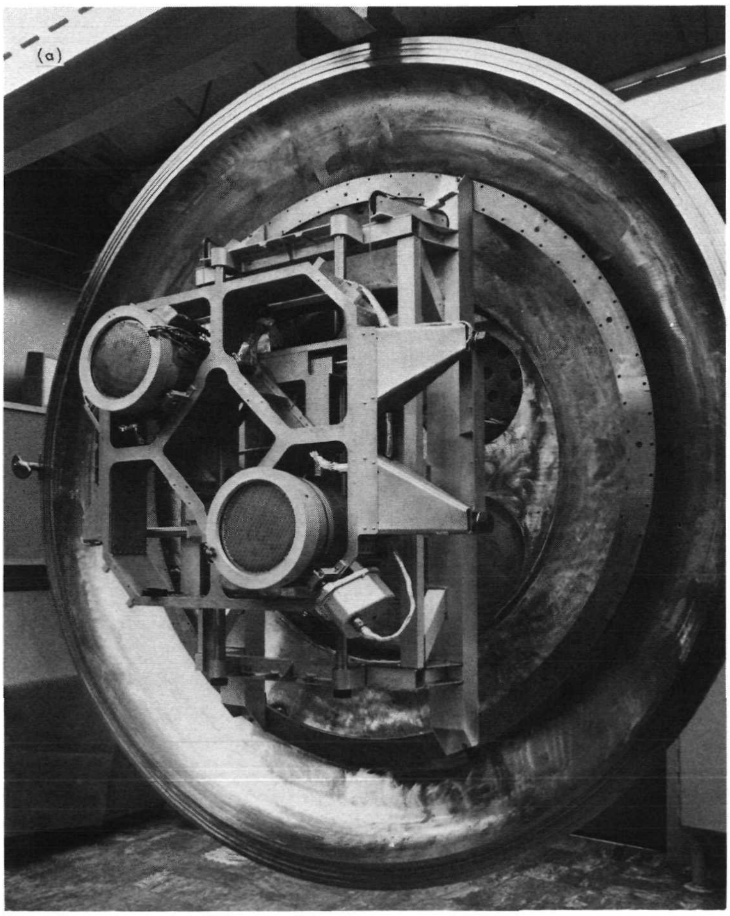

Fig. 5. SEPST III TVCS test configuration: (a) thruster array, (b) gimbal actuator, (c) translator actuator, (d) closed-loop control panel, (e) thrust vector control electronics breadboard

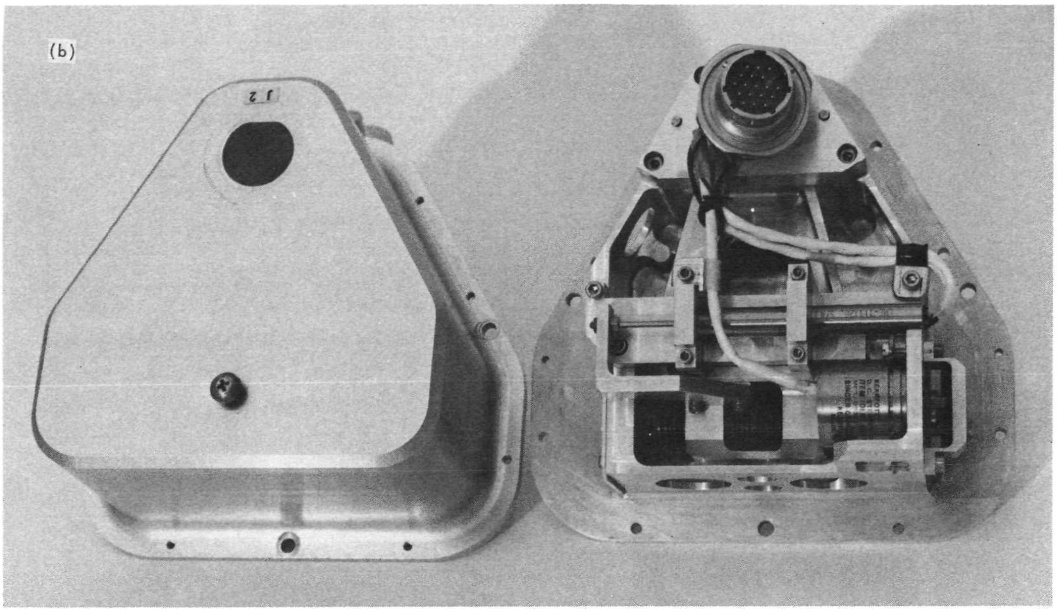

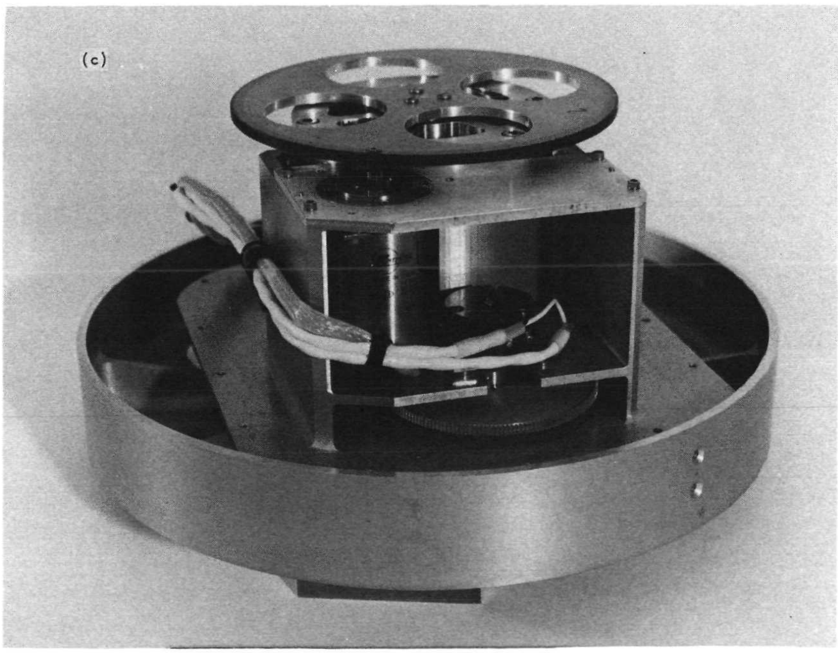

Fig. 5 (contd)

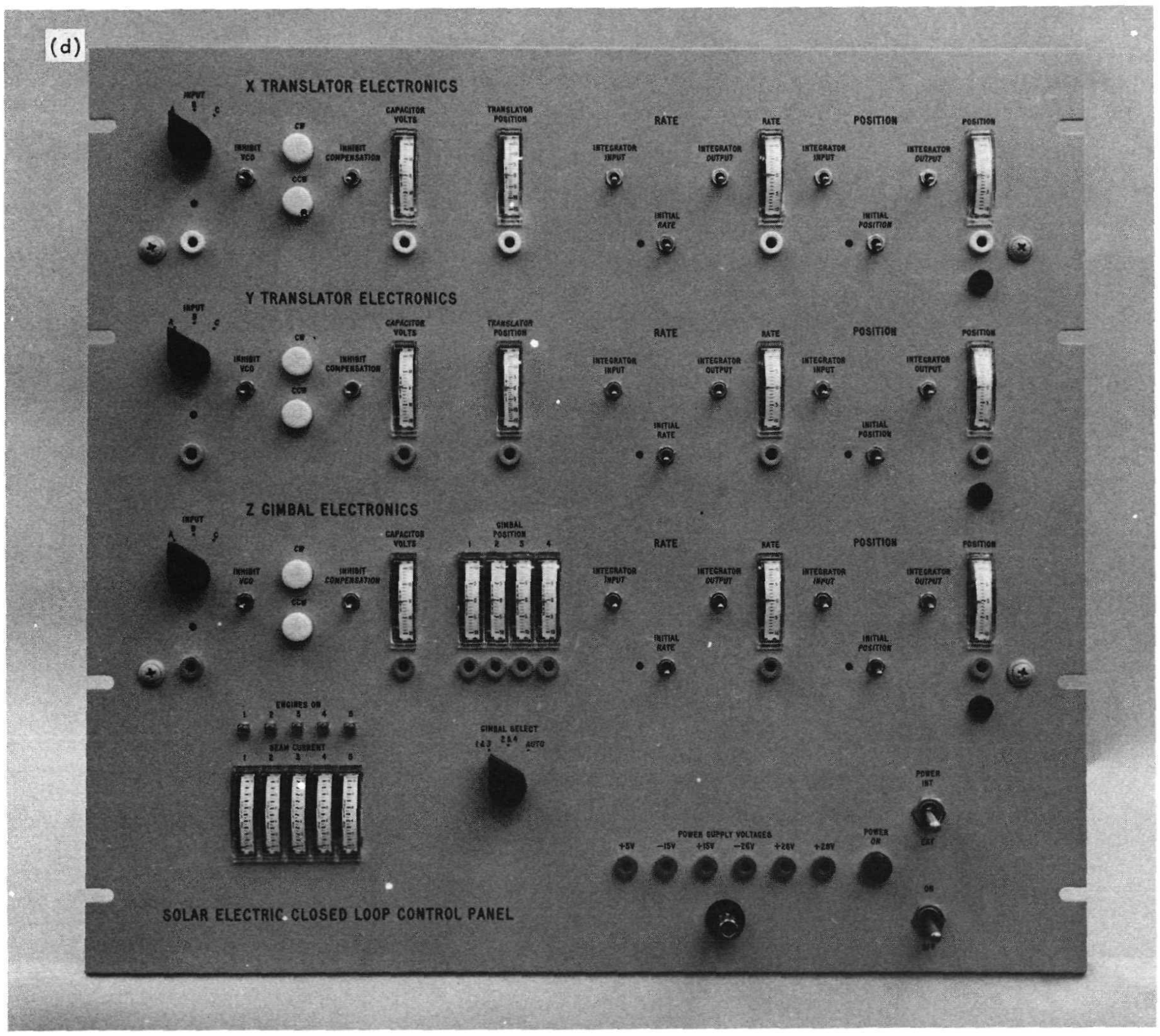
(d)
X TRANSLATOR ELECTRONICS
RATE
POSITION
Y TRANSLATOR ELECTRONICS
RATE
POSITION
Z GIMBAL ELECTRONICS
RATE
POSITION
SOLAR ELECTRIC CLOSED LOOP CONTROL PANEL

Fig. 5 (contd)

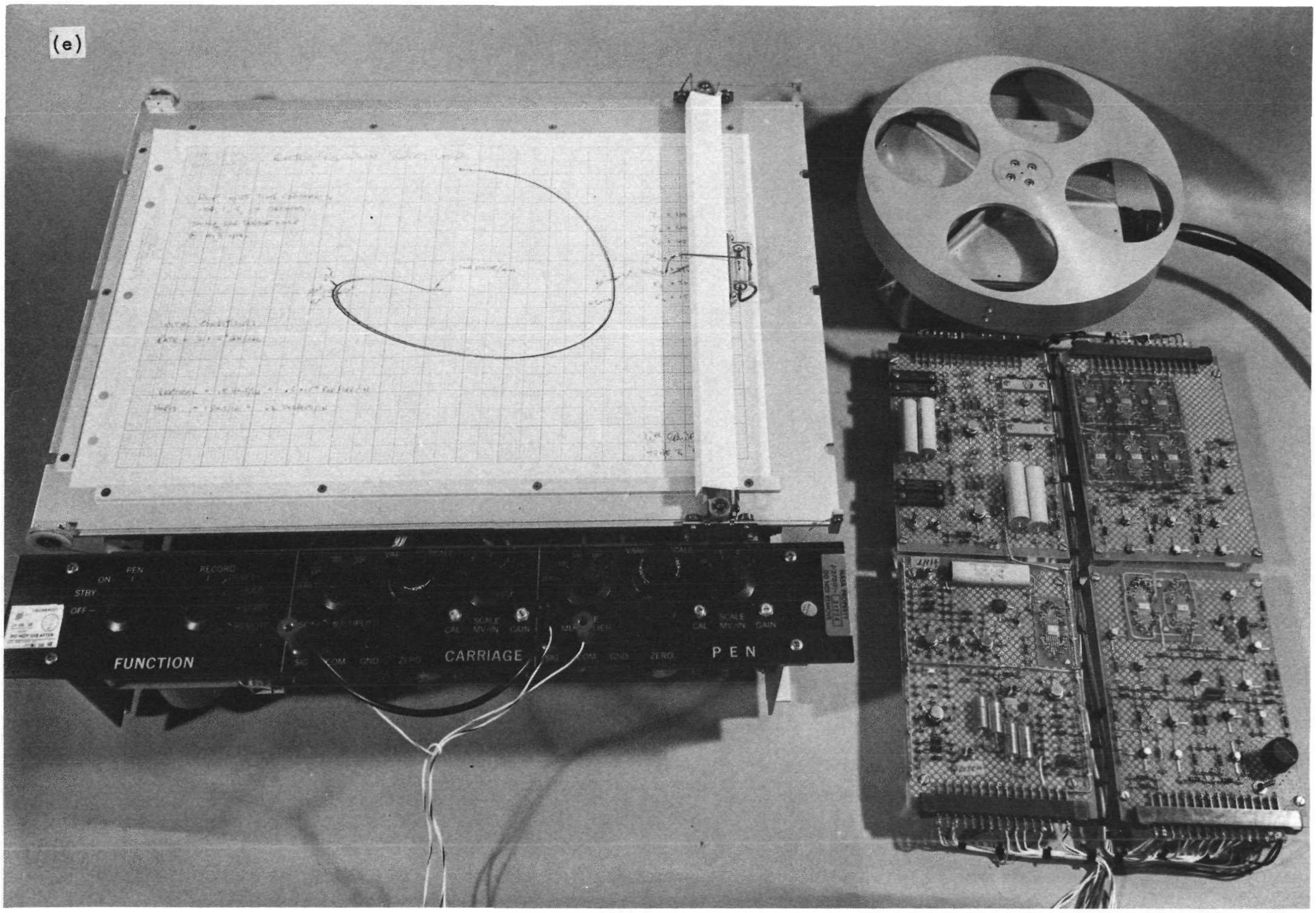

Fig. 5 (contd)

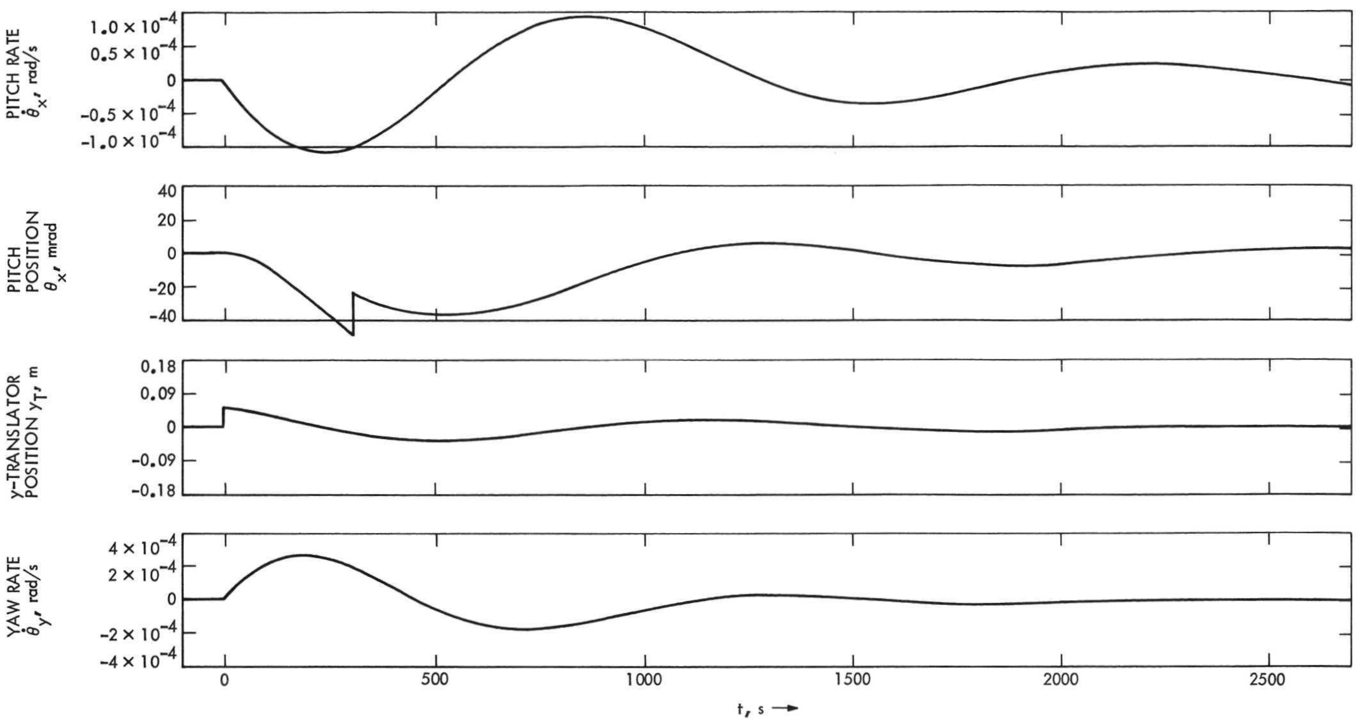

Fig. 6. TVCS test responses to initial translator and gimbal displacements (θ_x, θ_x, y_T, $\dot{\theta}_y$)

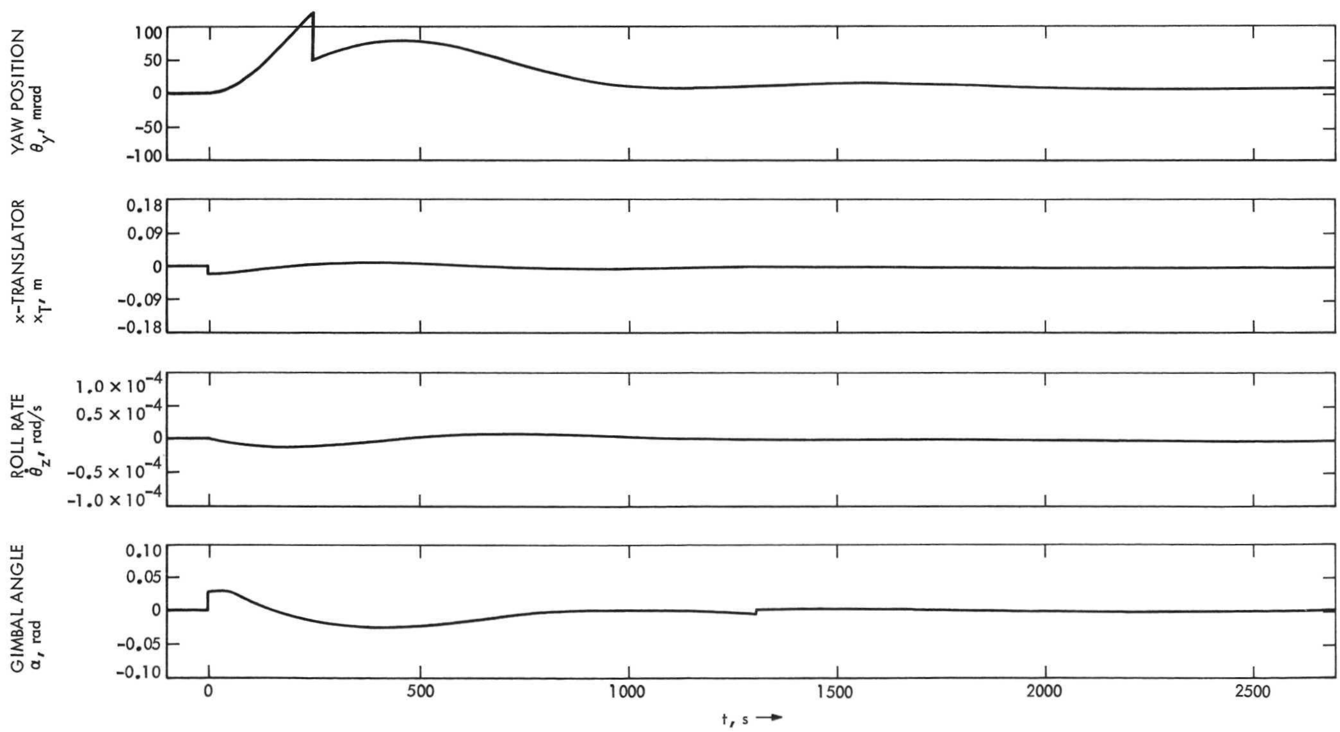

Fig. 7. TVCS test responses to initial translator and gimbal displacements (θ_y, x_T, $\dot{\theta}_z$ α)

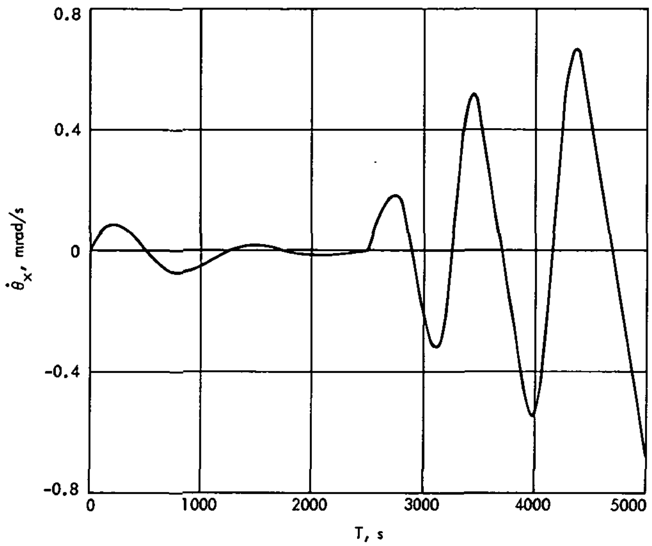

Fig. 8. $\dot{\theta}_x$ vs. time for engine-out transient at $t = 2500$ s

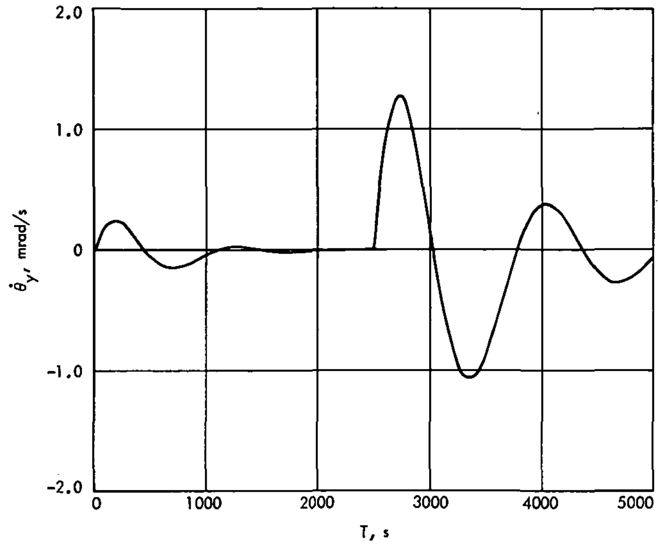

Fig. 10. $\dot{\theta}_y$ vs. time for engine-out transient at $t = 2500$ s

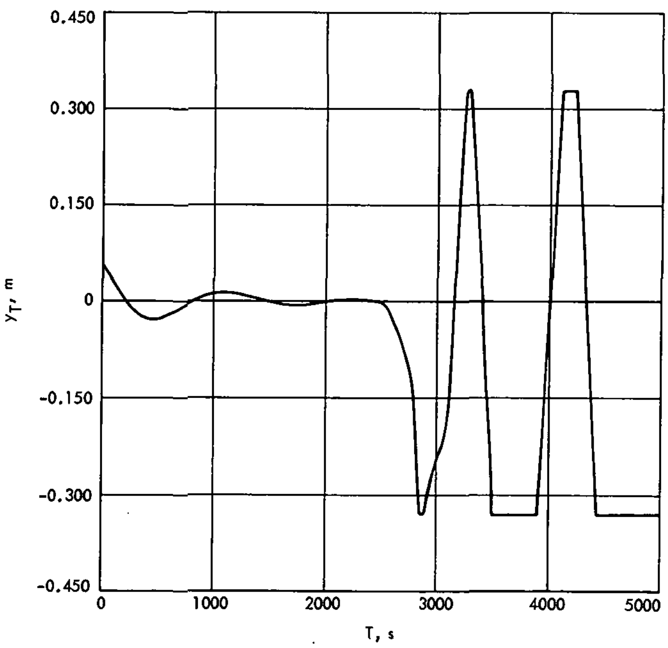

Fig. 9. y_T vs. time for engine-out transient at $t = 2500$ s

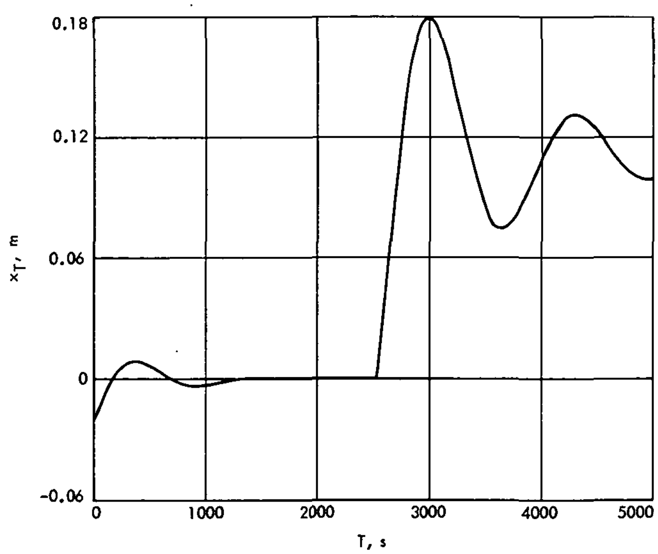

Fig. 11. x_T vs. time for engine-out transient at $t = 2500$ s

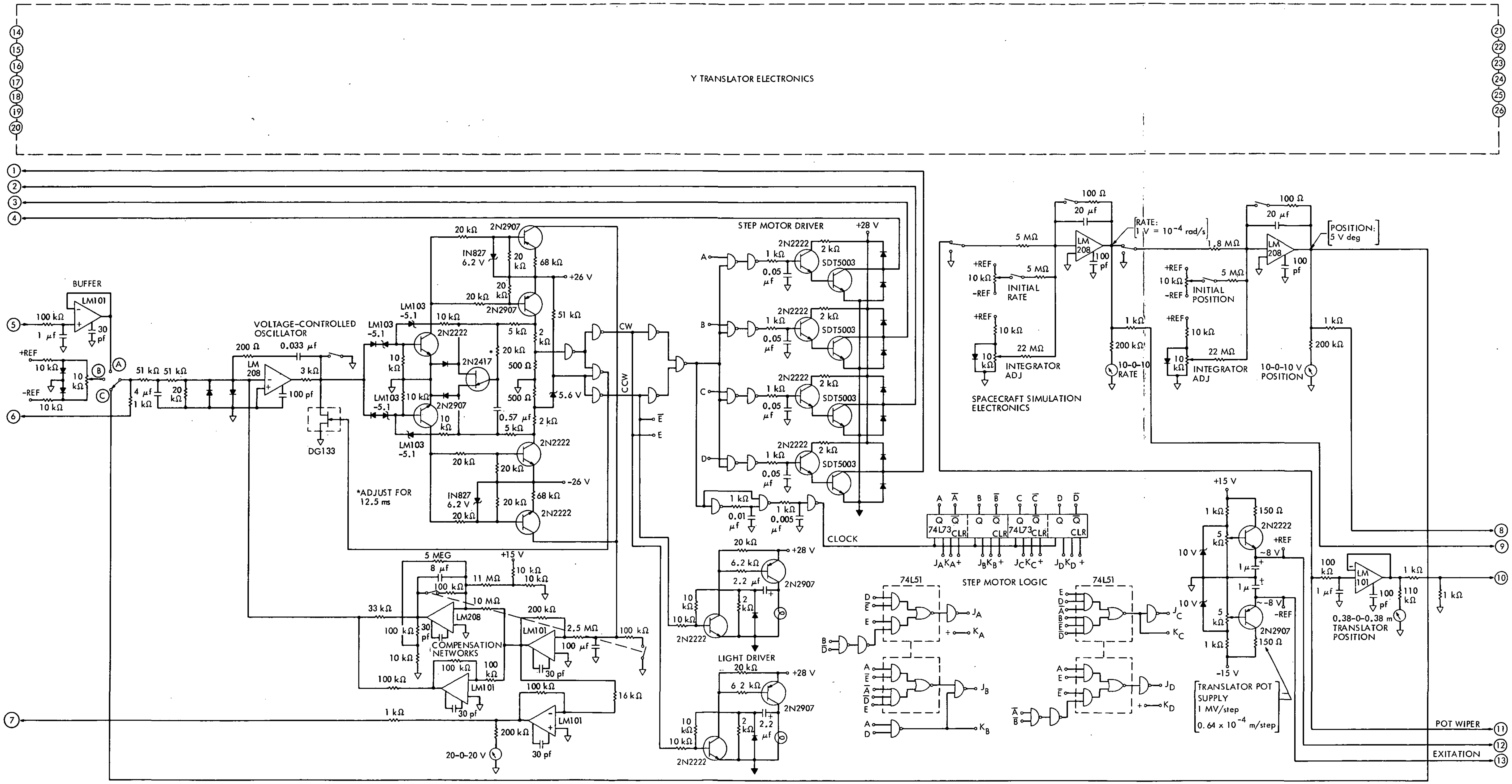

Fig. 12a. TVCS feedback compensation and VCO output circuitry

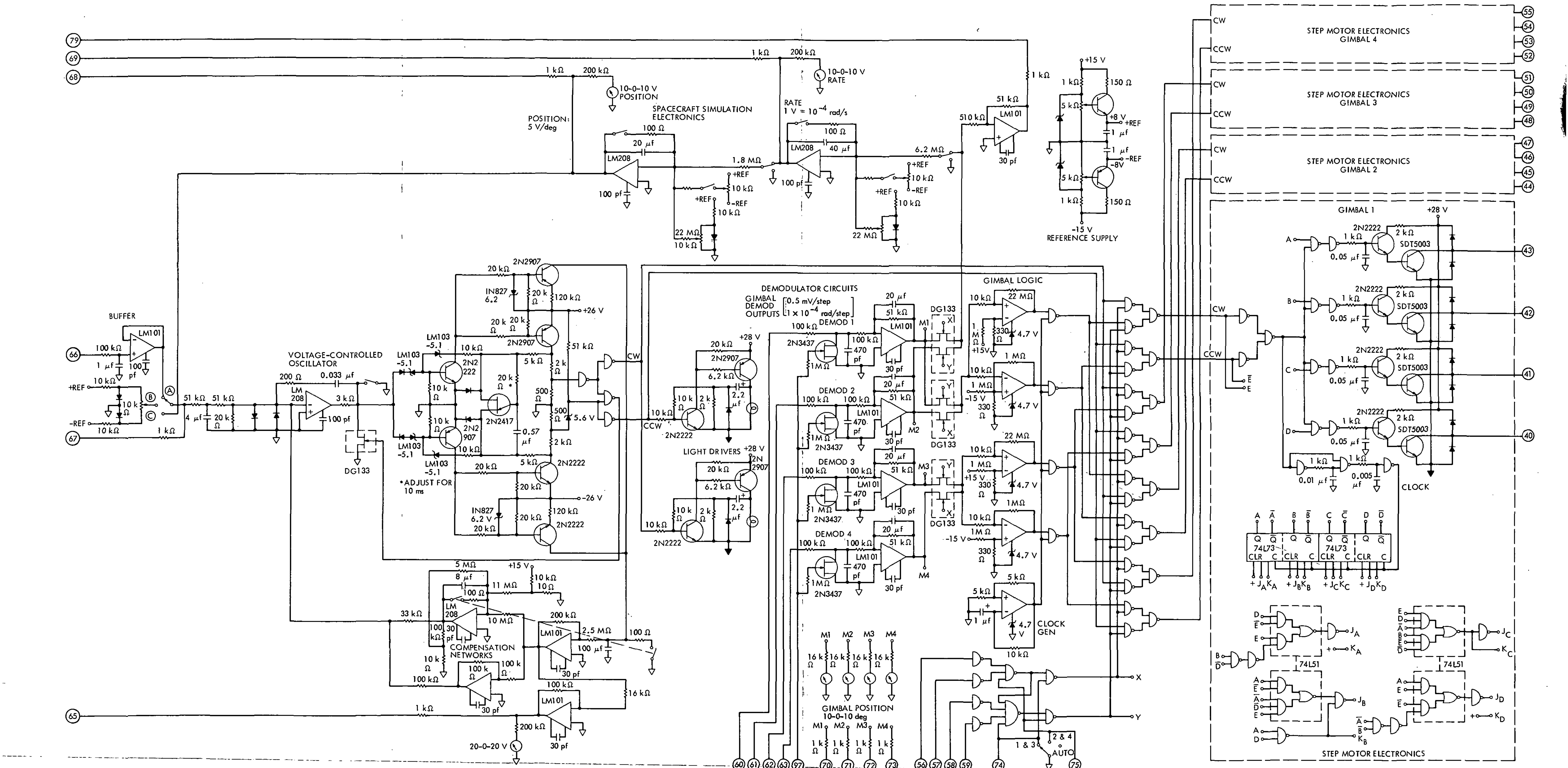

Fig. 12b. Translator control electronics

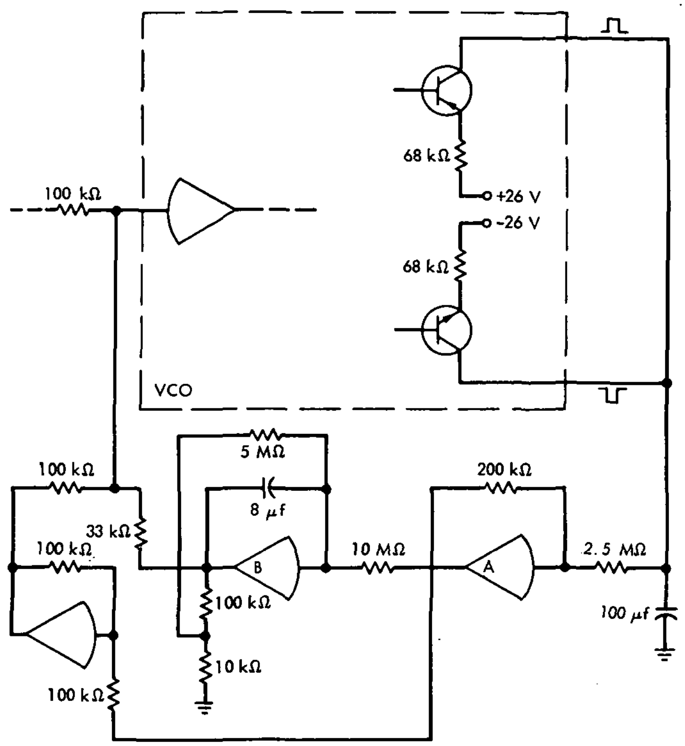

Fig. 12c. Gimbal control electronics

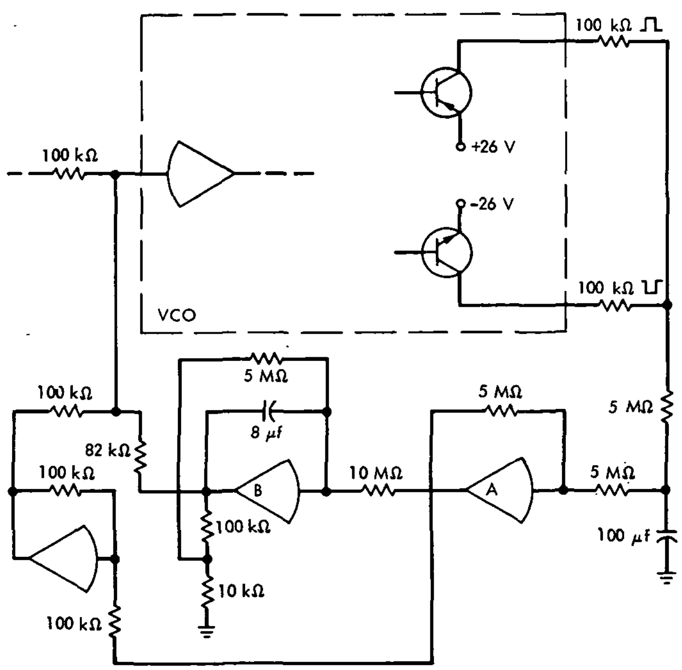

Fig. 12d. Modified TVCS feedback compensation and VCO output circuitry

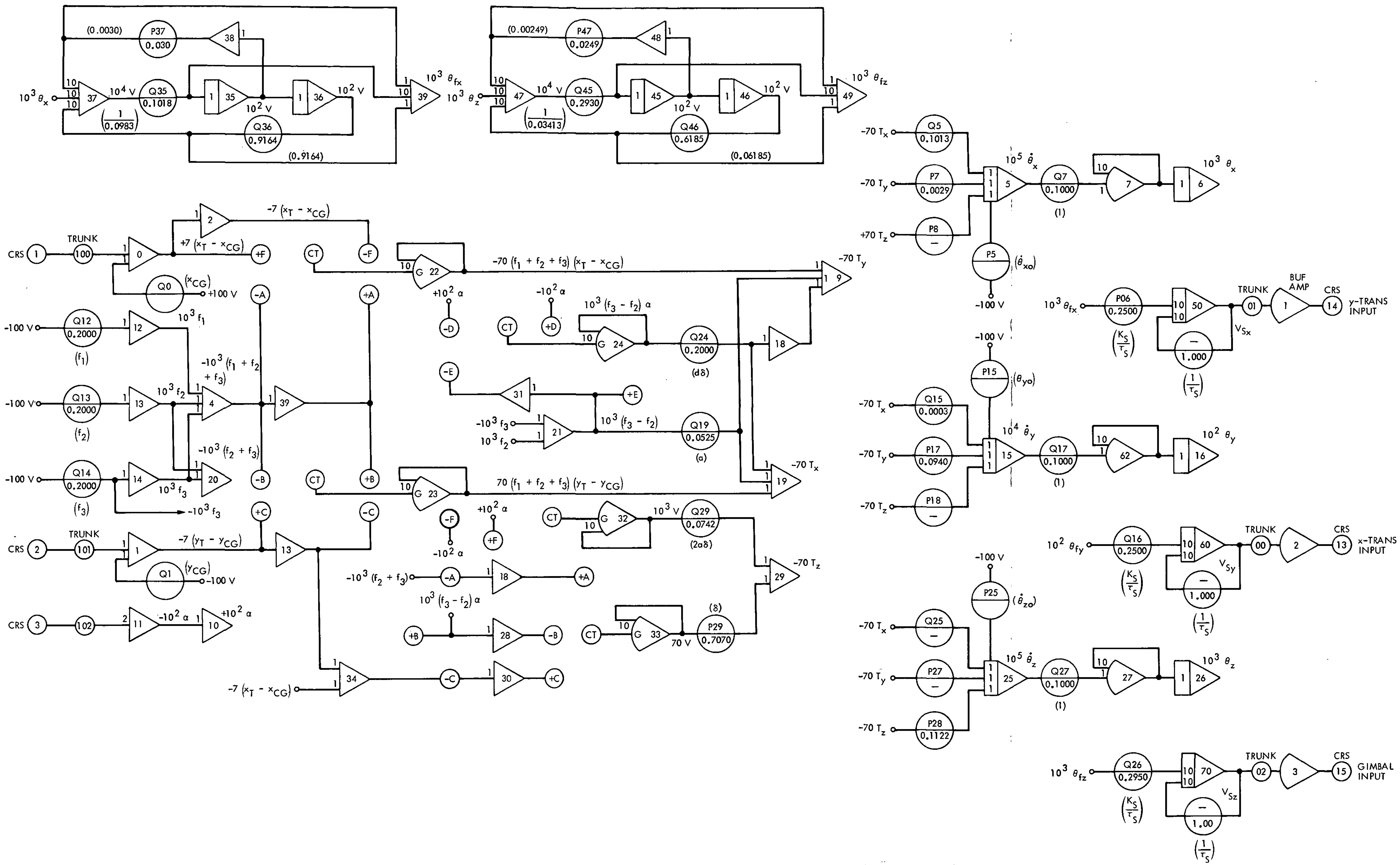

Fig. 13. SEPST III TVCS test analog computer program

Page Intentionally Left Blank

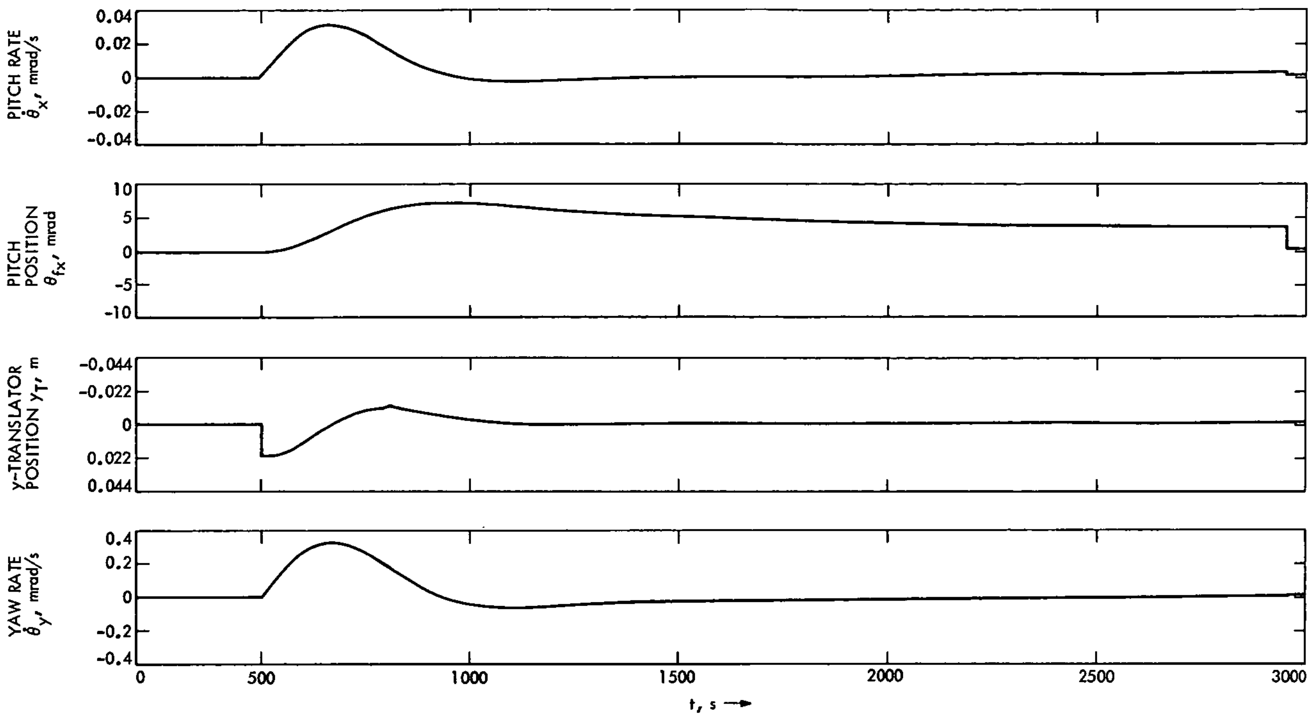

Fig. 14. TVCS (modified) test responses to initial translator and gimbal displacements ($\dot{\theta}_x$, θ_{fx}, y_T, $\dot{\theta}_y$)

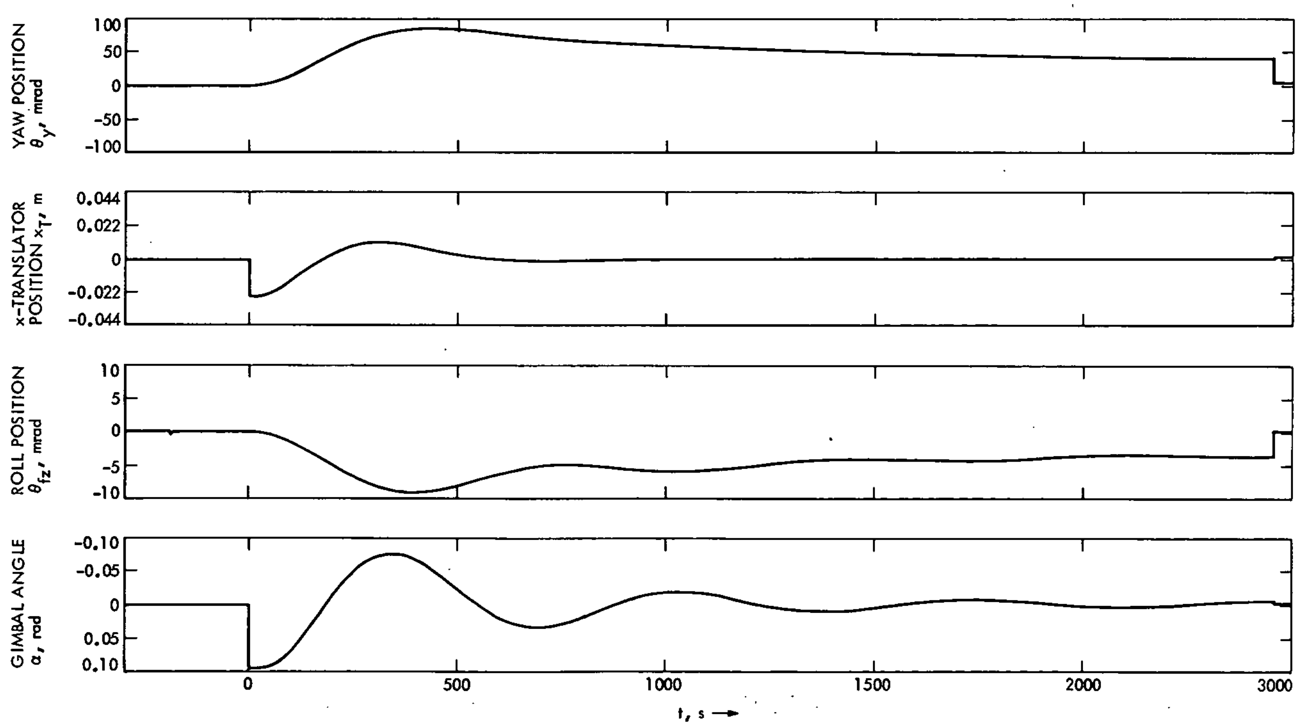

Fig. 15. TVCS (modified) test responses to initial translator and gimbal displacements (θ_y, x_T, θ_{fz}, α)

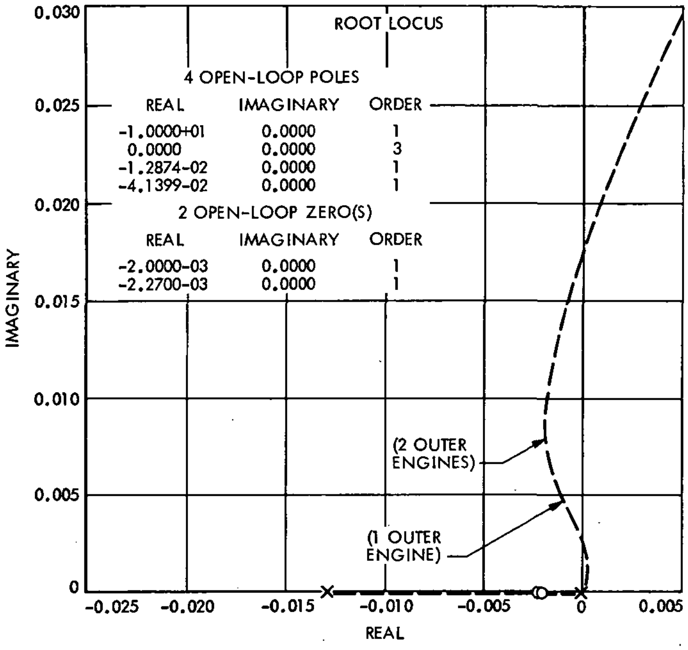

Fig. 16. Gimbaled axis closed-loop root loci for the TVCS test

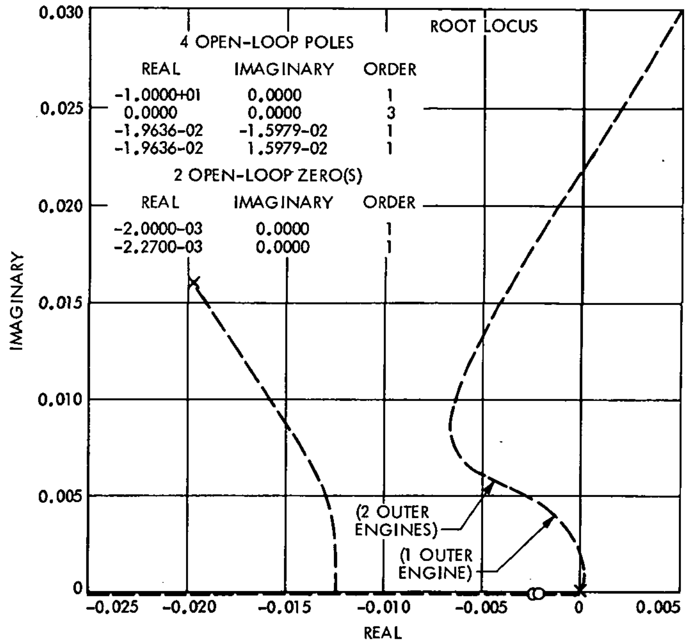

Fig. 17. Gimbaled axis closed-loop root loci using modified control parameters

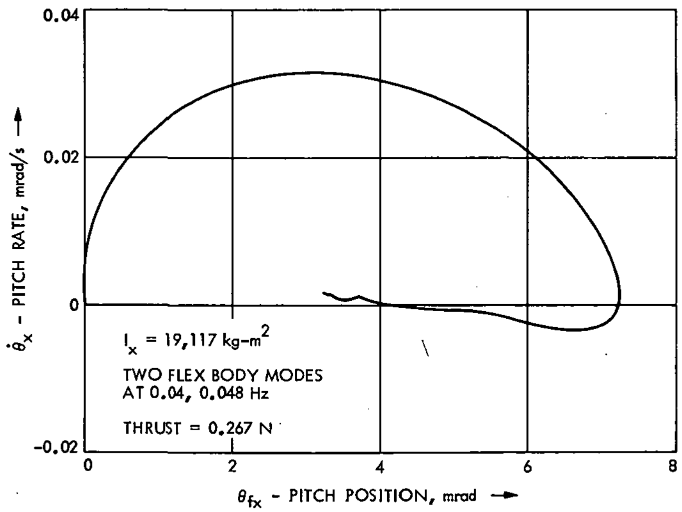

Fig. 18. SEPST III spacecraft pitch axis response to 0.02-m (0.07-ft) CG offset

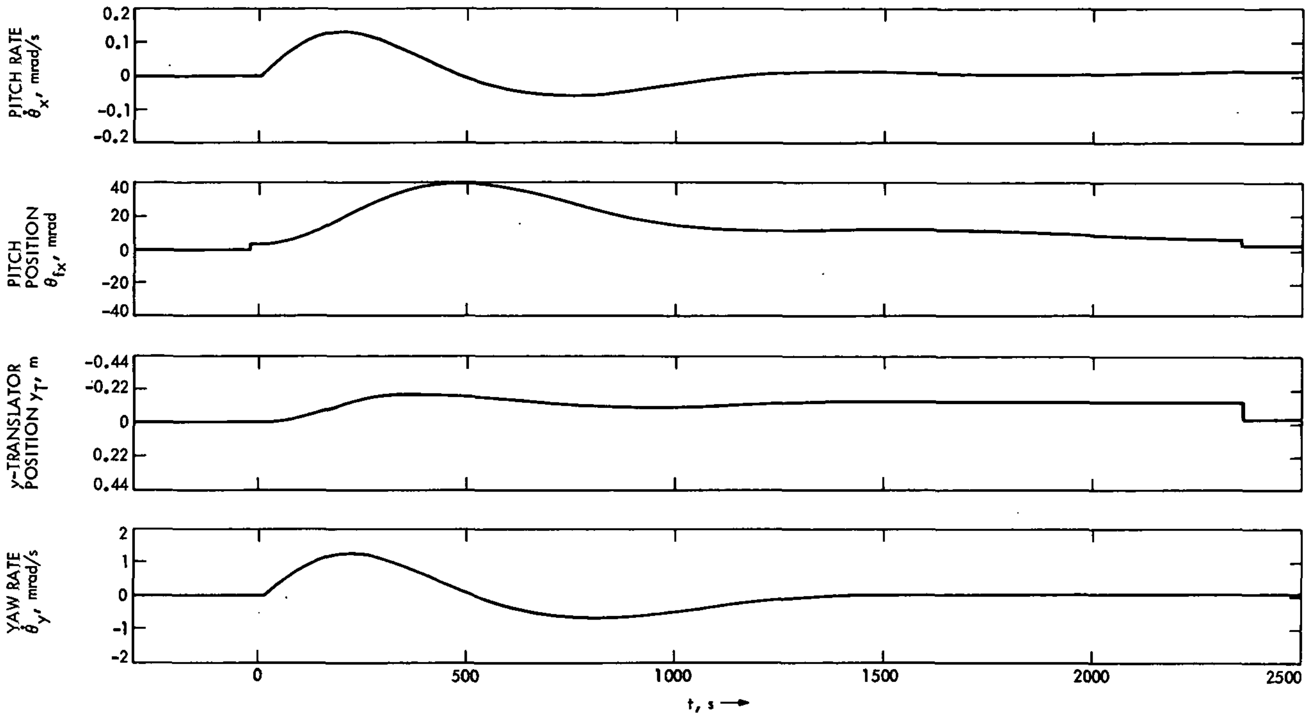

Fig. 19. TVCS test responses to engine-out ($f_2 = 0$) transient condition ($\dot{\theta}_x$, θ_{fx}, y_T, $\dot{\theta}_y$)

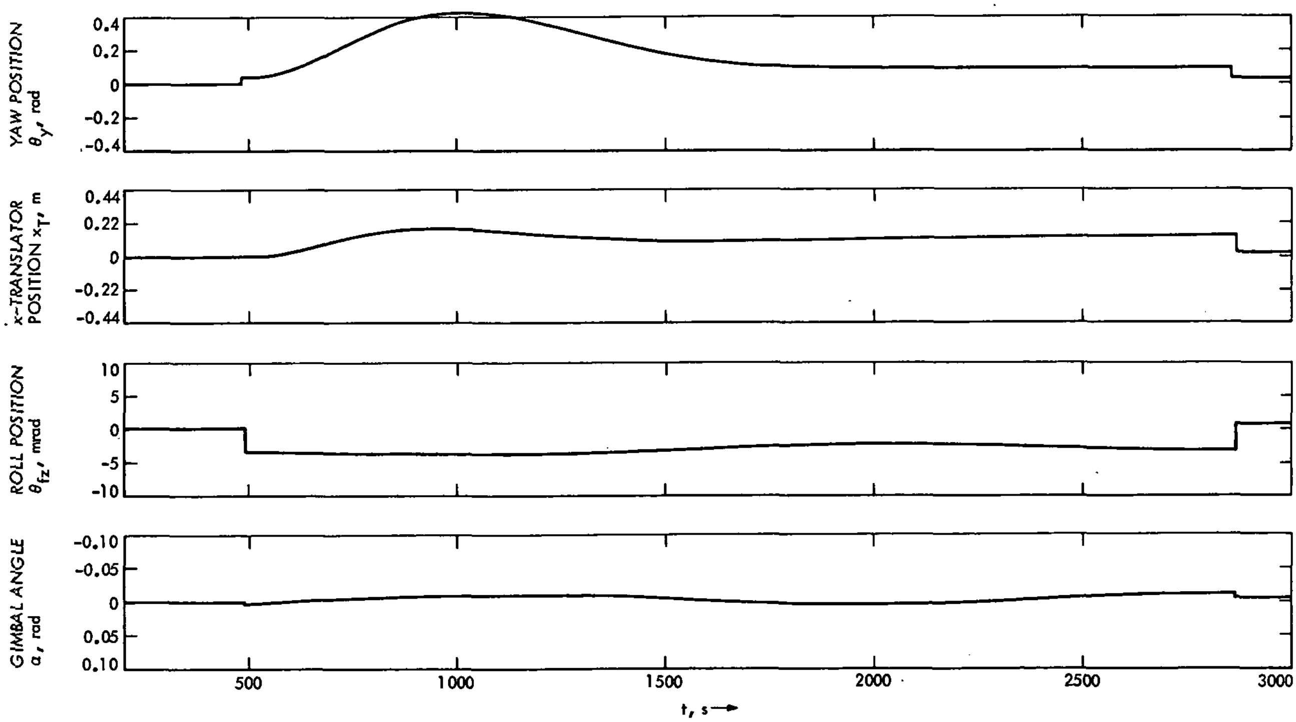

Fig. 20. TVCS test responses to engine-out ($f_2 = 0$) transient condition (θ_y, x_T, θ_{fz}, α)

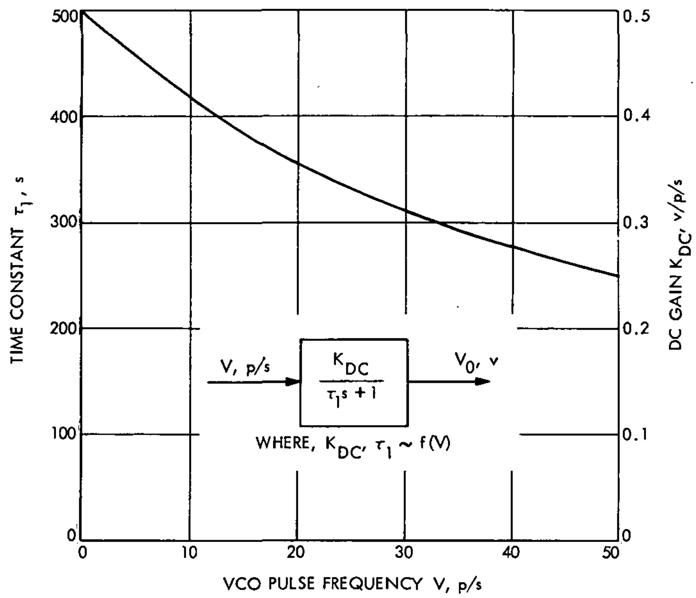

Fig. 21. Functional dependence of τ_1 lag on VCO pulse rate

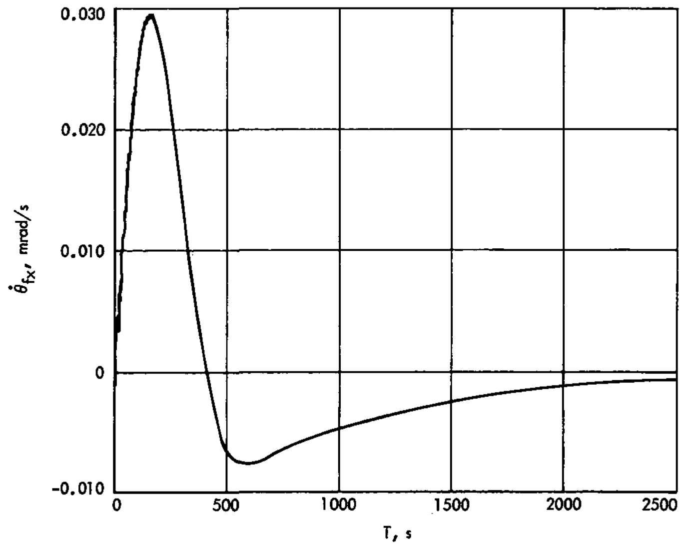

Fig. 23. $\dot{\theta}_{fx}$ vs. time, computer-simulated test response to initial translator and gimbal displacements

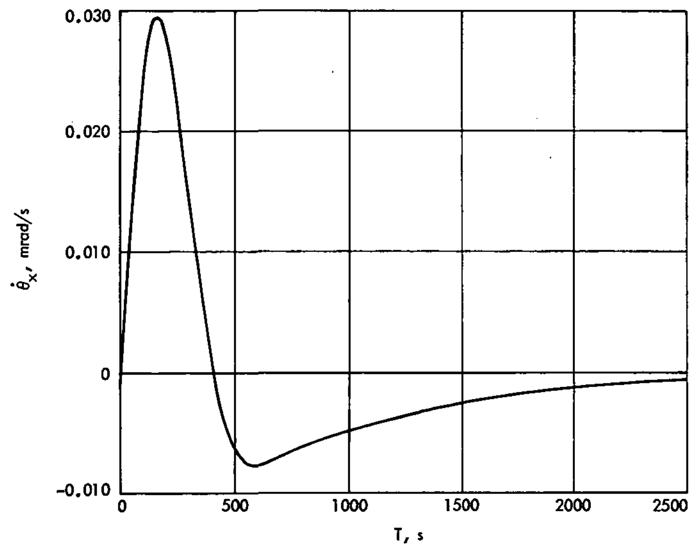

Fig. 22. $\dot{\theta}_x$ vs. time, computer-simulated test response to initial translator and gimbal displacements

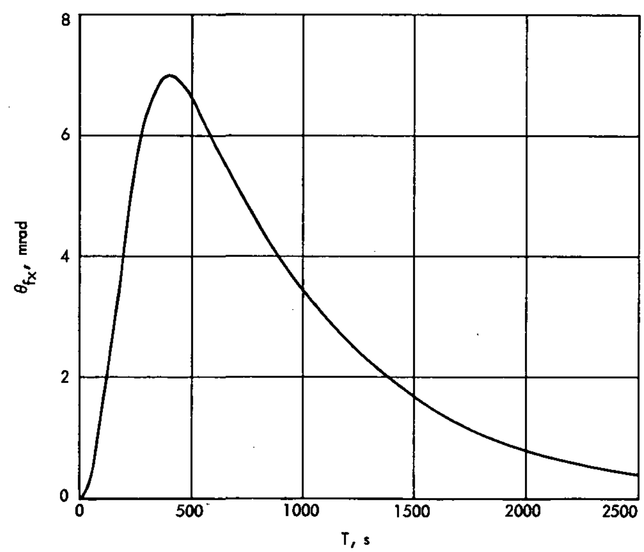

Fig. 24. θ_{fx} vs. time, computer-simulated test response to initial translator and gimbal displacements

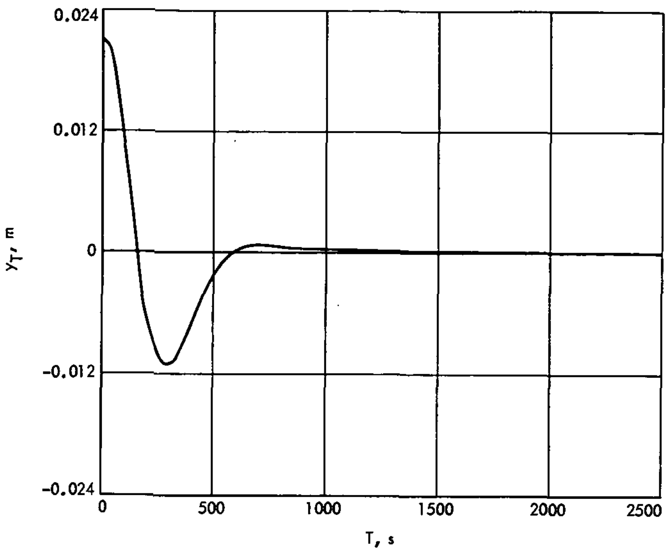

Fig. 25. y_T **vs. time, computer-simulated test response to initial translator and gimbal displacements**

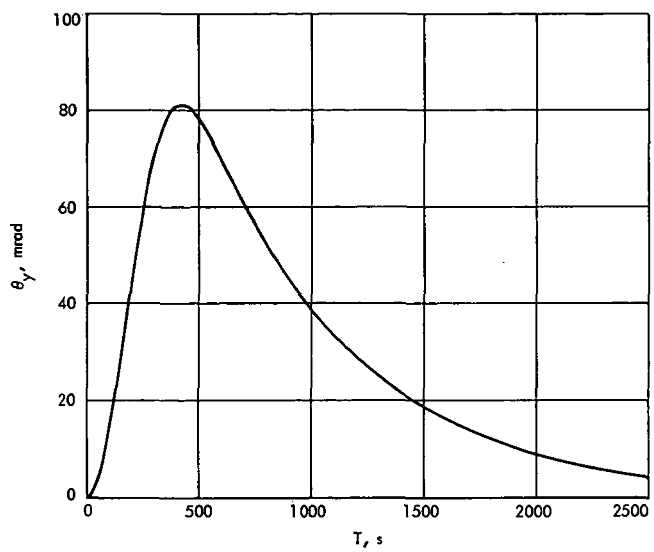

Fig. 27. θ_y **vs. time, computer-simulated test response to initial translator and gimbal displacements**

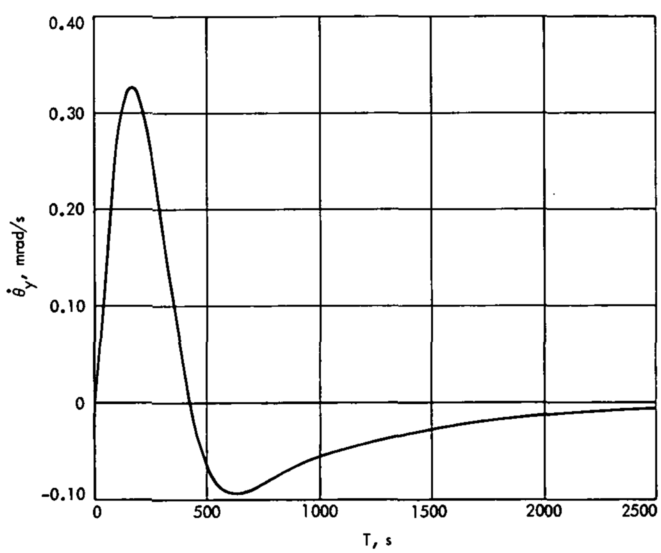

Fig. 26. $\dot{\theta}_y$ **vs. time, computer-simulated test response to initial translator and gimbal displacements**

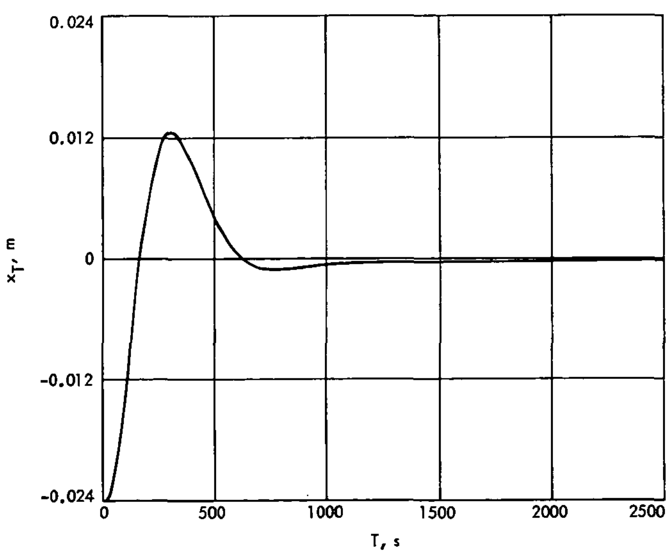

Fig. 28. x_T **vs. time, computer-simulated test response to initial translator and gimbal displacements**

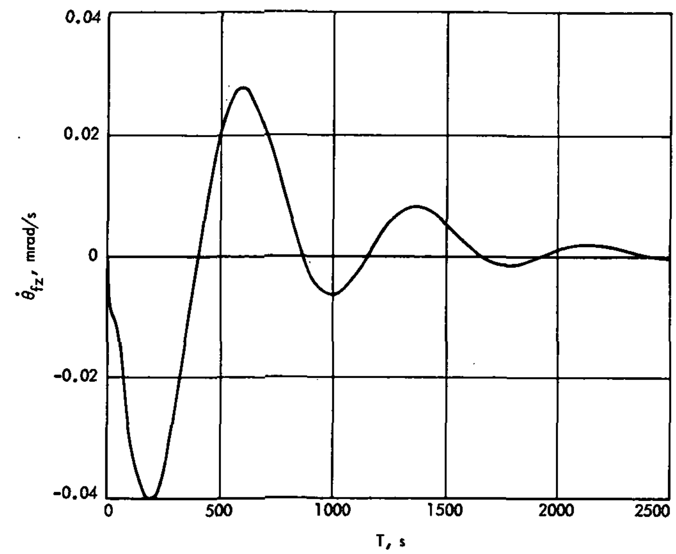

Fig. 29. $\dot{\theta}_{fz}$ vs. time, computer-simulated test response to initial translator and gimbal displacements

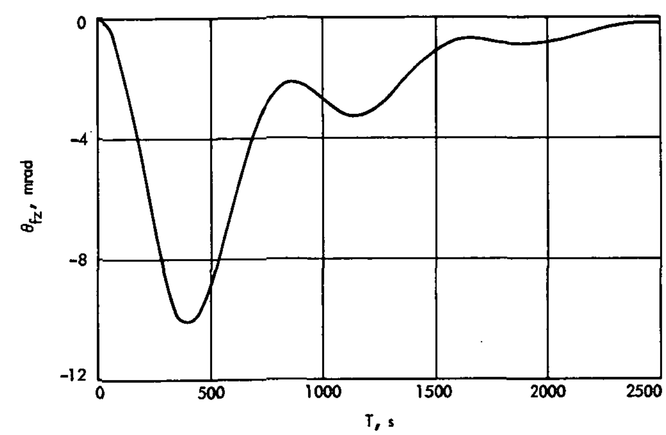

Fig. 30. θ_{fz} vs. time, computer-simulated test response to initial translator and gimbal displacements

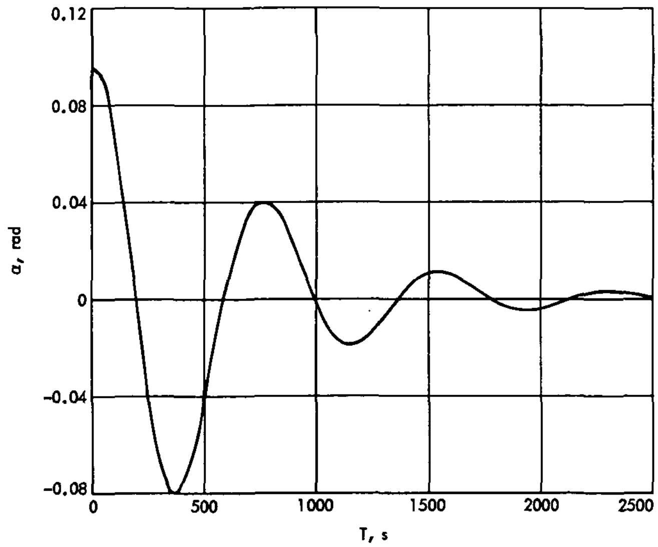

Fig. 31. α vs. time, computer-simulated test response to initial translator and gimbal displacements

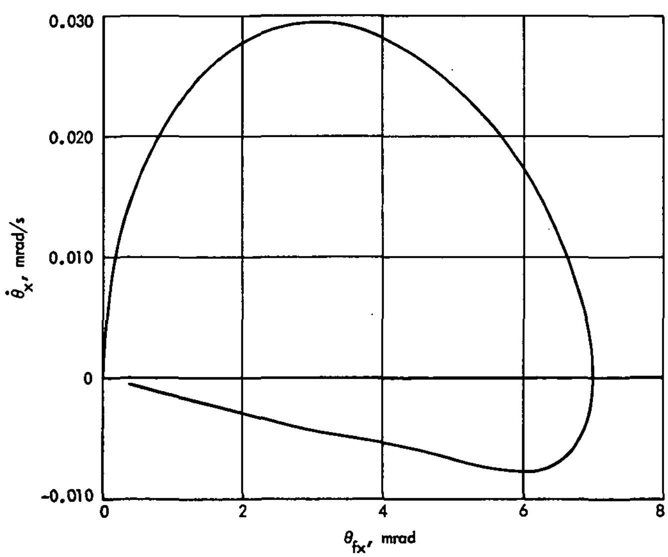

Fig. 32. $\dot{\theta}_x$ vs. θ_{fx}, computer-simulated test response to initial translator and gimbal displacements

"Page missing from available version"

PAGES → 35 — 42

MISSING.

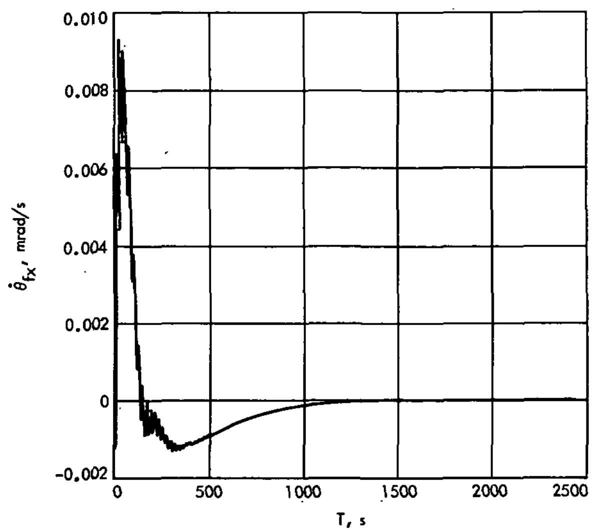

Fig. 53. $\dot{\theta}_{fx}$ **vs. time, simulated TVCS (with estimator) response to initial engine array offsets**

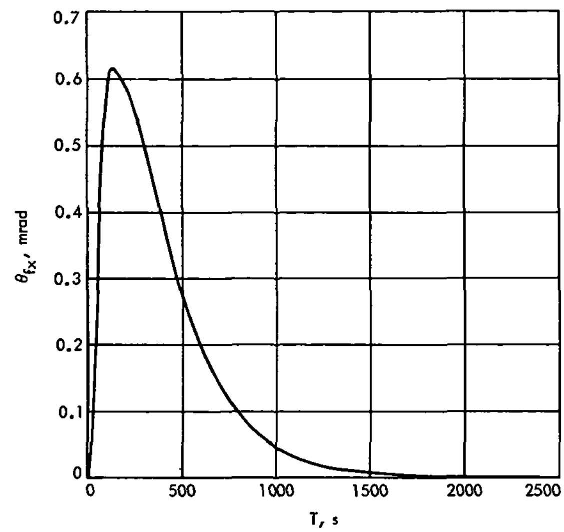

Fig. 54. θ_{fx} **vs. time, simulated TVCS (with estimator) response to initial engine array offsets**

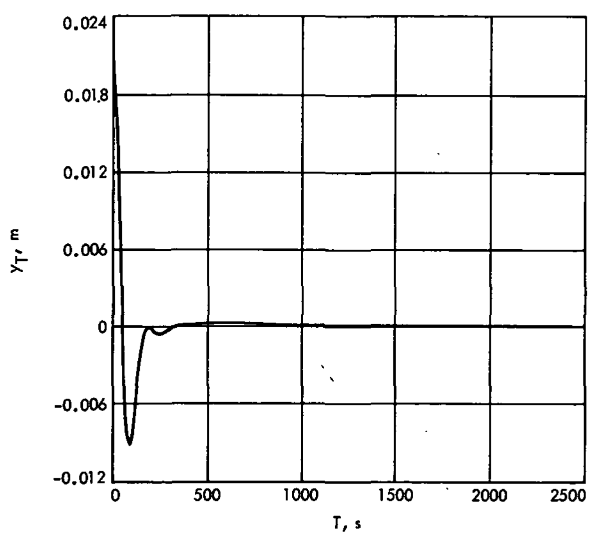

Fig. 55. y_T **vs. time, simulated TVCS (with estimator) response to initial engine array offsets**

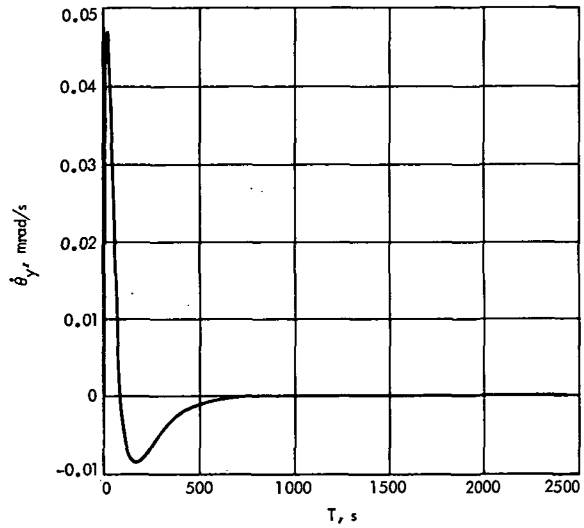

Fig. 56. $\dot{\theta}_y$ vs. time, simulated TVCS (with estimator) response to initial engine array offsets

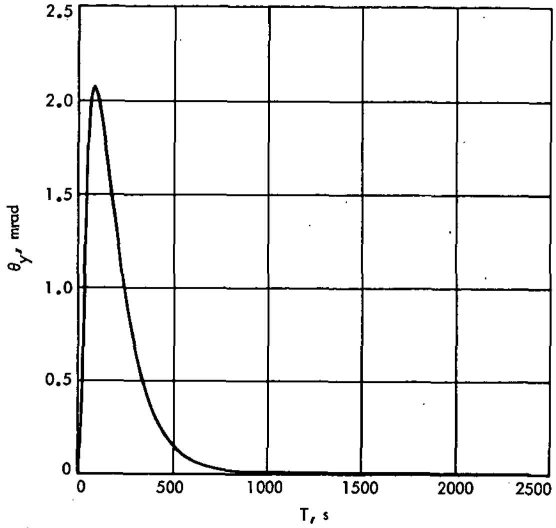

Fig. 57. θ_y vs. time, simulated TVCS (with estimator) response to initial engine array offsets

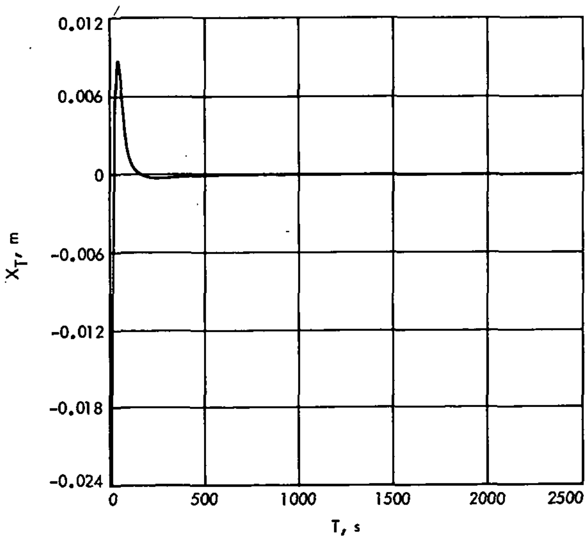

Fig. 58. x_T vs. time, simulated TVCS (with estimator) response to initial engine array offsets

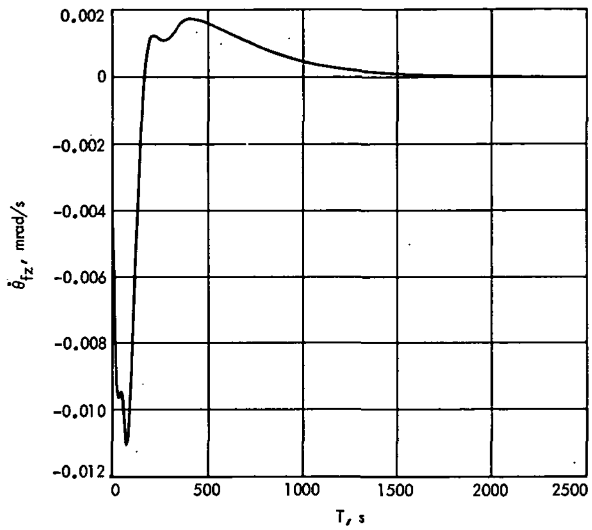

Fig. 59. $\dot{\theta}_{fz}$ **vs. time, simulated TVCS (with estimator) response to initial engine array offsets**

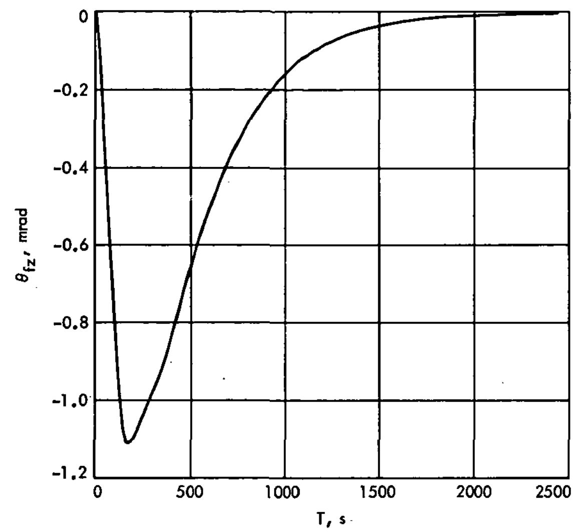

Fig. 60. θ_{fz} **vs. time, simulated TVCS (with estimator) response to initial engine array offsets**

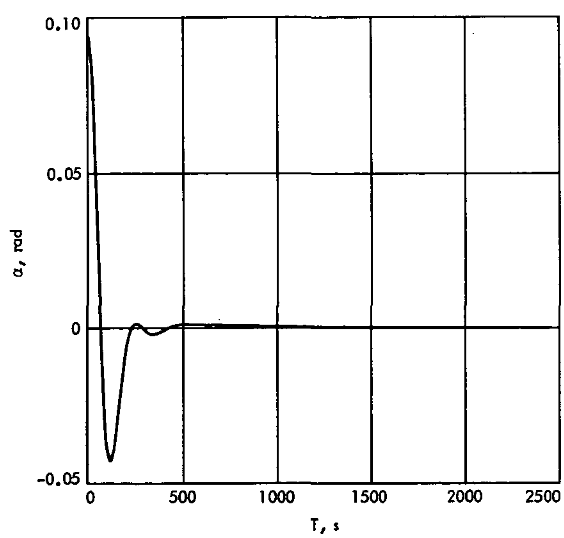

Fig. 61. α **vs. time, simulated TVCS (with estimator) response to initial engine array offsets**

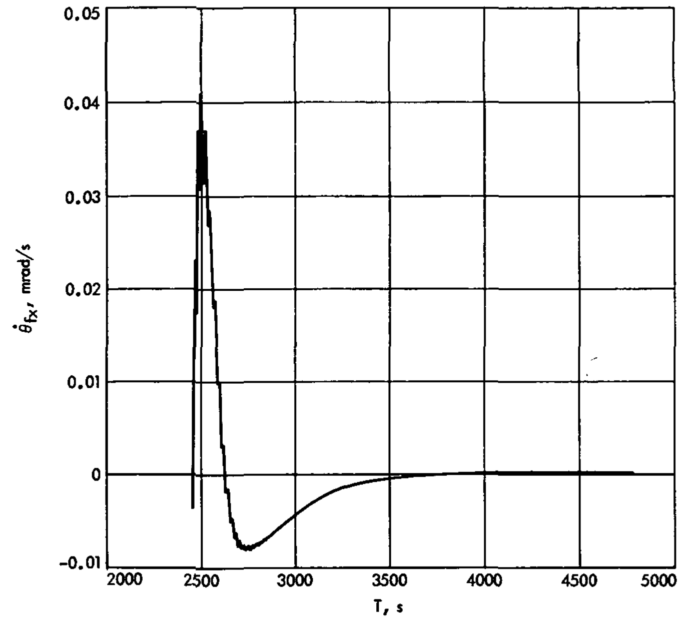

Fig. 62. $\dot{\theta}_{fx}$ vs. time, simulated TVCS (with estimator) response to engine-out transient

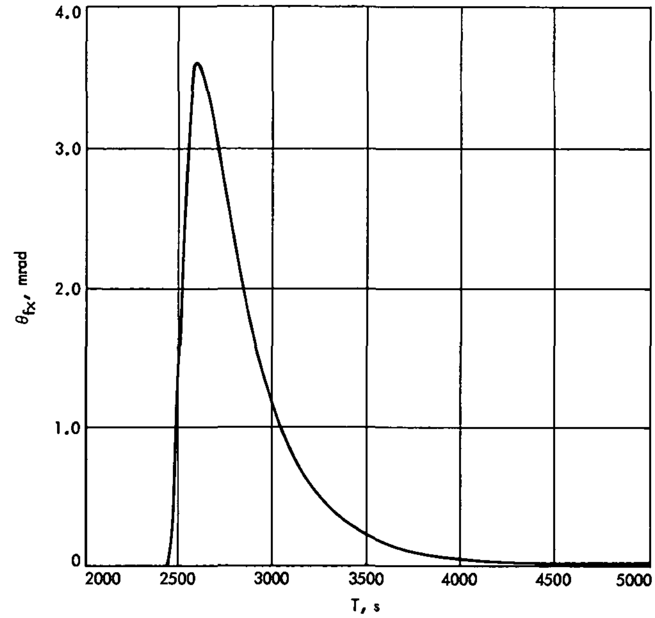

Fig. 63. θ_{fx} vs. time, simulated TVCS (with estimator) response to engine-out transient

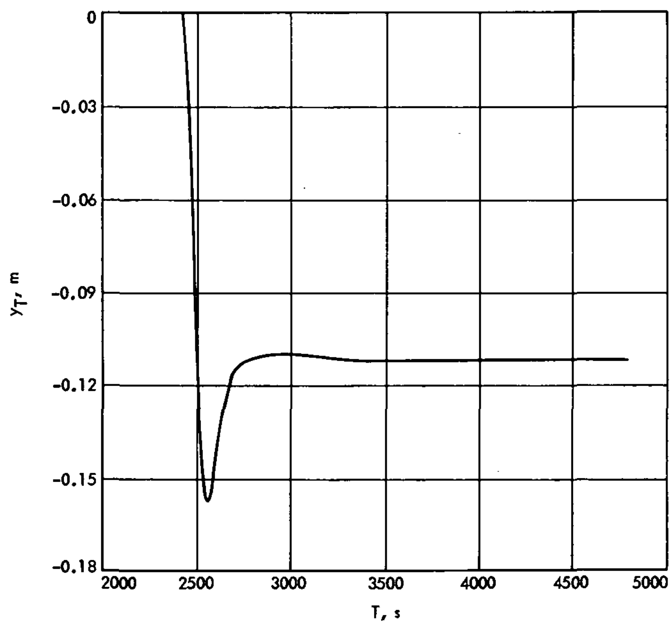

Fig. 64. y_T vs. time, simulated TVCS (with estimator) response to engine-out transient

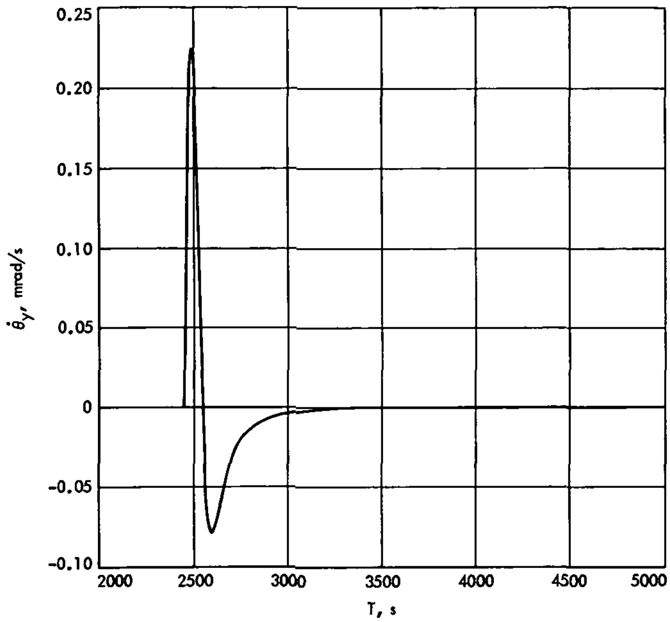

Fig. 65. $\dot{\theta}_y$ vs. time, simulated TVCS (with estimator) response to engine-out transient

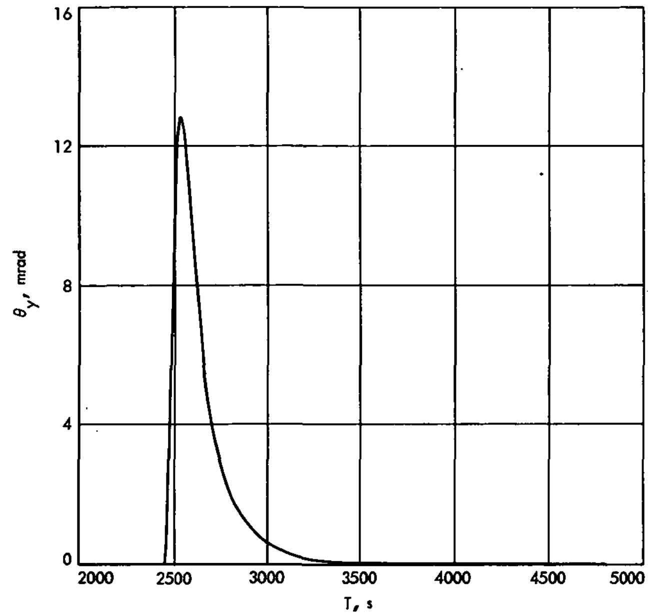

Fig. 66. θ_y vs. time, simulated TVCS (with estimator) response to engine-out transient

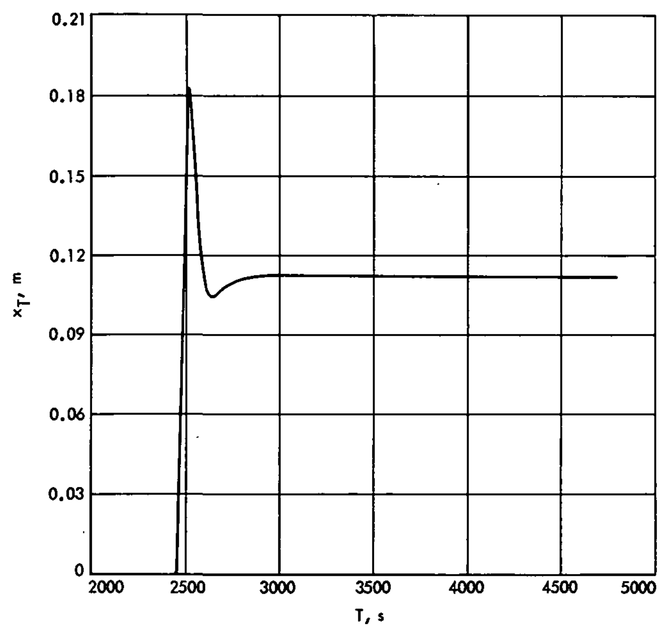

Fig. 67. x_T vs. time, simulated TVCS (with estimator) response to engine-out transient

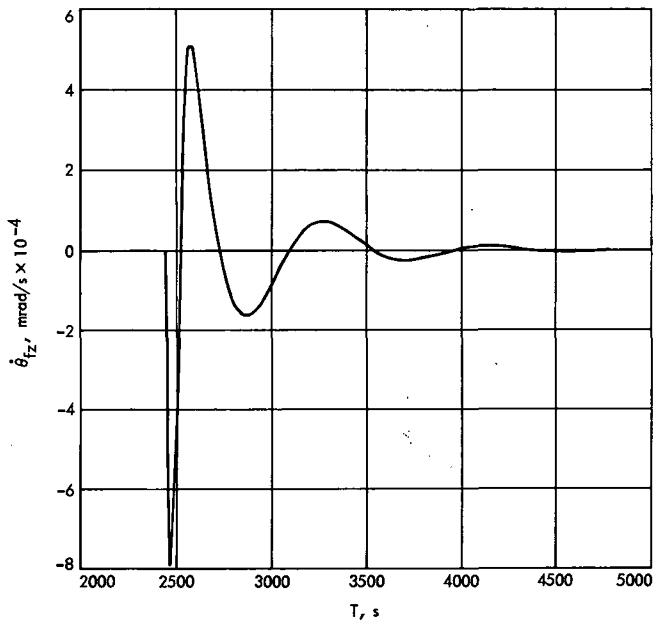

Fig. 68. $\dot{\theta}_{fz}$ **vs. time, simulated TVCS (with estimator) response to engine-out transient**

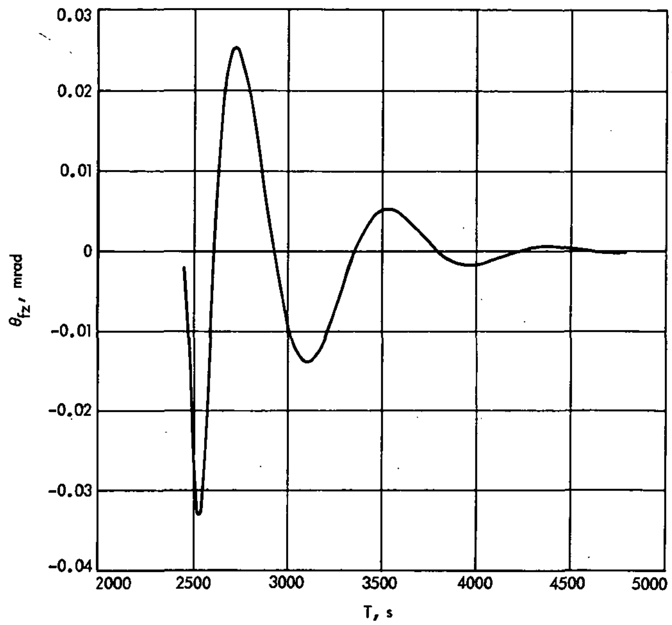

Fig. 69. θ_{fz} **vs. time, simulated TVCS (with estimator) response to engine-out transient**

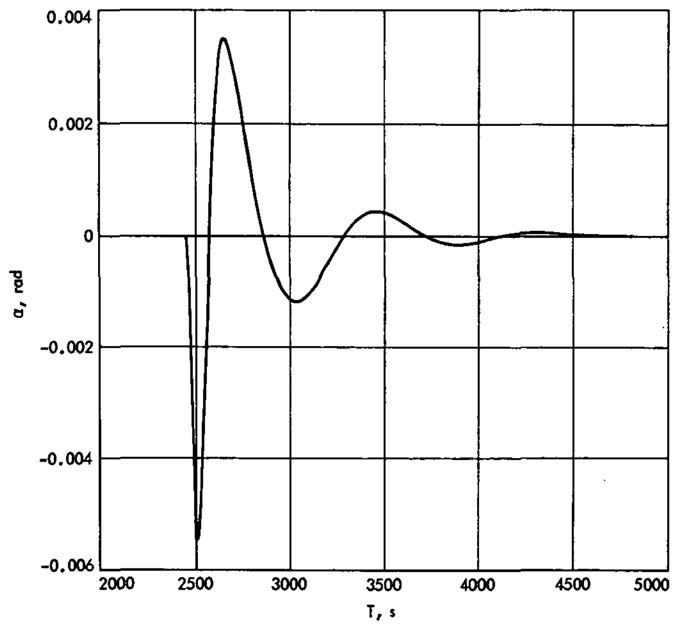

Fig. 70. α **vs. time, simulated TVCS (with estimator) response to engine-out transient**

```
PROGRAM   SOLAR ELECTRIC TVC (WITH RATE ESTIMATOR)
      TX=(F1+F2+F3)*(YT-YCG)+(F3-F2)*(A+ALP*D*DEL)
      TY=(F1+F2+F3)*(XCG-XT)+(F3-F2)*(A-ALP*D*DEL)
      TZ=(F3-F2)*(XT-XCG-YT+YCG)*ALP*DEL-(F2+F3)*2.*A*ALP*DEL
      THXDD=(I11*TX+I12*TY+I13*TZ)*1000.
      THYDD=(I12*TX+I22*TY+I23*TZ)*1000.
      THZDD=(I13*TX+I23*TY+I33*TZ)*1000.
      THXD=INTEG(THXDD,THXD0)
      THYD=INTEG(THYDD,THYD0)
      THZD=INTEG(THZDD,THZD0)
      THY=INTEG(THYD,0.)
     XXDD=(THXD-XX*(SIGX**2)-2.*ZETX*SIGX*XXD)/RX
     XZDD=(THZD-XZ*(SIGZ**2)-2.*ZETZ*SIGZ*XZD)/RZ
      XXD=INTEG(XXDD,0.)
      XZD=INTEG(XZDD,0.)
      XX=INTEG(XXD,0.)
      XZ=INTEG(XZD,0.)
     THFXD=XXDD+2.*ZETX*SIGX*XXD+(SIGX**2)*XX
     THFZD=XZDD+2.*ZETZ*SIGZ*XZD+(SIGZ**2)*XZ
      THFX=INTEG(THFXD,0.)
      THFZ=INTEG(THFZD,0.)
      THFXDE=INTEG((THFX-THFXE)/(2.*(B**2)),0.)
      THFXE=INTEG((THFXDE-(THFXE-THFX)/B),0.)
      THFZDE=INTEG((THFZ-THFZE)/(2.*(B**2)),0.)
      THFZE=INTEG((THFZDE-(THFZE-THFZ)/B),0.)
      THYDE=INTEG((THY-THYE)/(2.*(B**2)),0.)
      THYE=INTEG((THYDE-(THYE-THY)/B),0.)
      VXE=KSX*(THFXE+KRX*THFXDE)
      VYE=KSY*(THYE+KRY*THYDE)
      VZE=KSZ*(THFZE+KRZ*THFZDE)
      VCOXT=BOUND(-50.,50.,KVCOXT*(VYE-VFXT))
      VCOYT=BOUND(-50.,50.,KVCOYT*(VXE-VFYT))
      VCOG=BOUND(-50.,50.,KVCOG*(VZE-VFG))
      VFXT=INTEG((KFXT*VCOXT-VFXT)/T1XT,0.)
      VFYT=INTEG((KFYT*VCOYT-VFYT)/T1YT,0.)
      VFG=INTEG((KFG*VCOG-VFG)/T1G,0.)
      XT=LIMINT(KMXT*VCOXT,XT0,-1.1,1.1)
      YT=LIMINT(-KMYT*VCOYT,YT0,-1.1,1.1)
      ALP=LIMINT(KMA*VCOG,ALP0,-.2,.2)
      CINTERVAL  CI=5.0
      STPCLK   200.
      TERMT   (T.GE.FINTM)
CONSTANT B=1.,KFXT=.30,KFYT=.20,KFG=.175
CONSTANT T1XT=100.,T1YT=200.,T1G=250.
CONSTANT KRX=200.,KRY=100.,KRZ=250.
CONSTANT F1=.020,F3=.020,F2=.020
CONSTANT  XCG=0.,YCG=0.
CONSTANT  A=.75,D=4.,DEL=.7071
CONSTANT I11=.709089E-4,I12=-.95843E-7,I13=-.292855E-7
CONSTANT I22=.658164E-3,I23=-.202686E-5,I33=.785683E-4
CONSTANT  THXD0=0.,THYD0=0.,THZD0=0.
CONSTANT KSX=.250,KSY=.2500,KSZ=.295
CONSTANT KVCOXT=50.,KVCOYT=50.,KVCOG=50.
CONSTANT KMXT=2.08E-4,KMYT=2.08E-4,KMA=.97E-4
CONSTANT XT0=-.0800,YT0=.070,ALP0=.095
CONSTANT RX=.0983,RZ=.03413
CONSTANT SIGX=.3027,SIGZ=.2487
CONSTANT ZETX=.005,ZETZ=.005
CONSTANT FINTM=2450.
      OUTPUT  20,XXD,THY,XZD,THXD,THYD,THZD,XT,YT,ALP,VCOXT,VCOYT,...
     THFXD,THFZD,VCOG,                                        THFX,THFZ
      PREPAR XT,YT,ALP,THFXD,THYD,THFZ,THFX,THY,THFZD,THXD
END
```

Fig. 71. Simulation program for rate-estimating TVCS

NASA — JPL — Coml., L.A., Calif.